CLNS 08/2018
CLEO 08-02

Dalitz plot analysis of the $D^+ \to K^-\pi^+\pi^+$ decay

G. Bonvicini,[1] D. Cinabro,[1] M. Dubrovin,[1] A. Lincoln,[1] P. Naik,[2] J. Rademacker,[2] D. M. Asner,[3] K. W. Edwards,[3] J. Reed,[3] R. A. Briere,[4] T. Ferguson,[4] G. Tatishvili,[4] H. Vogel,[4] M. E. Watkins,[4] J. L. Rosner,[5] J. P. Alexander,[6] D. G. Cassel,[6] J. E. Duboscq,[6] R. Ehrlich,[6] L. Fields,[6] L. Gibbons,[6] R. Gray,[6] S. W. Gray,[6] D. L. Hartill,[6] B. K. Heltsley,[6] D. Hertz,[6] J. M. Hunt,[6] J. Kandaswamy,[6] D. L. Kreinick,[6] V. E. Kuznetsov,[6] J. Ledoux,[6] H. Mahlke-Krüger,[6] D. Mohapatra,[6] P. U. E. Onyisi,[6] J. R. Patterson,[6] D. Peterson,[6] D. Riley,[6] A. Ryd,[6] A. J. Sadoff,[6] X. Shi,[6] S. Stroiney,[6] W. M. Sun,[6] T. Wilksen,[6] S. B. Athar,[7] R. Patel,[7] J. Yelton,[7] P. Rubin,[8] B. I. Eisenstein,[9] I. Karliner,[9] S. Mehrabyan,[9] N. Lowrey,[9] M. Selen,[9] E. J. White,[9] J. Wiss,[9] R. E. Mitchell,[10] M. R. Shepherd,[10] D. Besson,[11] T. K. Pedlar,[12] D. Cronin-Hennessy,[13] K. Y. Gao,[13] J. Hietala,[13] Y. Kubota,[13] T. Klein,[13] B. W. Lang,[13] R. Poling,[13] A. W. Scott,[13] P. Zweber,[13] S. Dobbs,[14] Z. Metreveli,[14] K. K. Seth,[14] A. Tomaradze,[14] J. Libby,[15] A. Powell,[15] G. Wilkinson,[15] K. M. Ecklund,[16] W. Love,[17] V. Savinov,[17] A. Lopez,[18] H. Mendez,[18] J. Ramirez,[18] J. Y. Ge,[19] D. H. Miller,[19] I. P. J. Shipsey,[19] B. Xin,[19] G. S. Adams,[20] M. Anderson,[20] J. P. Cummings,[20] I. Danko,[20] D. Hu,[20] B. Moziak,[20] J. Napolitano,[20] Q. He,[21] J. Insler,[21] H. Muramatsu,[21] C. S. Park,[21] E. H. Thorndike,[21] F. Yang,[21] M. Artuso,[22] S. Blusk,[22] S. Khalil,[22] J. Li,[22] R. Mountain,[22] S. Nisar,[22] K. Randrianarivony,[22] N. Sultana,[22] T. Skwarnicki,[22] S. Stone,[22] J. C. Wang,[22] and L. M. Zhang[22]

(CLEO Collaboration)

[1] *Wayne State University, Detroit, Michigan 48202, USA*
[2] *University of Bristol, Bristol BS8 1TL, UK*
[3] *Carleton University, Ottawa, Ontario, Canada K1S 5B6*
[4] *Carnegie Mellon University, Pittsburgh, Pennsylvania 15213, USA*
[5] *Enrico Fermi Institute, University of Chicago, Chicago, Illinois 60637, USA*
[6] *Cornell University, Ithaca, New York 14853, USA*
[7] *University of Florida, Gainesville, Florida 32611, USA*
[8] *George Mason University, Fairfax, Virginia 22030, USA*
[9] *University of Illinois, Urbana-Champaign, Illinois 61801, USA*
[10] *Indiana University, Bloomington, Indiana 47405, USA*
[11] *University of Kansas, Lawrence, Kansas 66045, USA*
[12] *Luther College, Decorah, Iowa 52101, USA*
[13] *University of Minnesota, Minneapolis, Minnesota 55455, USA*
[14] *Northwestern University, Evanston, Illinois 60208, USA*
[15] *University of Oxford, Oxford OX1 3RH, UK*
[16] *State University of New York at Buffalo, Buffalo, New York 14260, USA*
[17] *University of Pittsburgh, Pittsburgh, Pennsylvania 15260, USA*
[18] *University of Puerto Rico, Mayaguez, Puerto Rico 00681*
[19] *Purdue University, West Lafayette, Indiana 47907, USA*
[20] *Rensselaer Polytechnic Institute, Troy, New York 12180, USA*
[21] *University of Rochester, Rochester, New York 14627, USA*
[22] *Syracuse University, Syracuse, New York 13244, USA*

(Dated: February 27, 2008)

Abstract

We perform a Dalitz plot analysis of $D^+ \to K^-\pi^+\pi^+$ decay with the CLEO-c data set of 572 pb^{-1} of e^+e^- collisions accumulated at the $\psi(3770)$. This corresponds to 1.6 million D^+D^- pairs from which we select 140793 candidate events with a small background of $\sim$1.1%. We compare our results with previous measurements using the isobar model. We modify the isobar model with improved description of some of the contributing resonances, and get better agreement with our data. We also consider a quasi-model-independent approach and measure the magnitude and phase of the contributing $K\pi$ S wave in the range of invariant masses from the threshold to the maximum in this decay. This gives an improved descriptions of our data over the isobar model. Finally we allow for an isospin-two $\pi^+\pi^+$ S-wave contribution, and find that adding this to both the isobar model and quasi-model independent approach gives the best description of our data.

I. INTRODUCTION

In comparison to other D^+ meson modes, the $D^+ \to K^-\pi^+\pi^+$ decay is unique in many aspects. The large branching fraction, $\mathcal{B}(D^+ \to K^-\pi^+\pi^+) = (9.51 \pm 0.34)\%$, for this Cabibbo favored mode makes it the usual choice for normalization of other D^+ meson decay rates. Understanding its peculiar intermediate substructure will be beneficial. The only obvious contribution to this decay, observed in the $K\pi$-mass spectrum, is $K^*(892)^0\pi^+$, which comprises merely 12% of the total rate. A large contribution of over 60% from a $K\pi$ S-wave intermediate state has been observed in earlier experiments, including MARK III [1], NA14 [2], E691 [3], E687 [4], and E791 [5, 6], where the $D^+ \to K^-\pi^+\pi^+$ decay has been studied with the Dalitz plot technique [7]. Hence, the $D^+ \to K^-\pi^+\pi^+$ decay is a good laboratory to study $K\pi$ S-wave dynamics. The previous analysis by E791 [5] achieved good agreement with their data by including a low-mass $K^-\pi^+$ scalar resonance, κ, that significantly redistributed all fit fractions (FF) observed by earlier experiments. This particular model, even though it is based on the largest data set, has been excluded from the world average given in the PDG [8].

The two identical pions in the final state should obey Bose symmetry. Assuming that the three body decay is dominated by two-body intermediate states, there would be two identical $K^-\pi^+$ waves interfering with each other. This symmetry significantly reduces the degrees of freedom in the regular Dalitz plot analysis and allows the application of a model-independent partial wave analysis [6]. We would also expect a small contribution from the isospin-two $\pi^+\pi^+$ S wave, which exhibits non-trivial dynamics as observed in scattering experiments [9].

The data used in this analysis was accumulated with the CLEO-c detector [10]. Our event sample is based on 572 pb^{-1} of e^+e^- collisions at $\sqrt{s} \simeq 3770$ MeV, produced by the Cornell Electron Storage Ring (CESR). This sample corresponds to the production of $\sim$1.6 million D^+D^- pairs in the process $e^+e^- \to \psi(3770) \to D^+D^-$. We select 140793 $D^+ \to K^-\pi^+\pi^+$ candidate events for the Dalitz plot analysis (charge conjugation is implied throughout this paper). Our sample is very clean with a background fraction of about 1.1%, and is nine times larger than the dataset used by E791. The invariant mass resolution in this three-track D-meson decay is very good, $\sim$2.5 MeV/c^2. It is improved by a kinematic fit requiring a three-track common vertex with the D meson mass constraint. Our experimental conditions are similar to those of MARK III, where D mesons are produced with small momentum.

There has been significant theoretical interest in this decay, sparked by the large, low-mass $K\pi$ S-wave contribution [11–13]. These authors reanalyze the E791 data with their own models. E791 later reinterpreted their own data with a model-independent partial wave analysis [6], and we apply this in our analysis with minor modifications.

In Section II we briefly discuss CLEO-c experimental techniques, giving the event selection for the Dalitz plot, fits to the efficiency and estimations of the background. The formalism we use for the amplitude parameterization in this analysis is described in Section III. In Section IV we compare our results with the best previous measurements by E791 [5], and try to improve the isobar model in order to get a better description of our data. Finally, we apply a quasi-model-independent partial wave analysis, following Ref. [6], and measure the partial waves contributing to this decay in Section V. Systematic cross-checks are considered in Section VI. We discuss results and outstanding issues of this analysis in Section VII, and summarize our results in Section VIII.

II. DETECTOR AND EXPERIMENTAL TECHNIQUE

CLEO-c is a general purpose detector which includes a tracking system for measuring momenta and specific ionization of charged particles, a Ring Imaging Cherenkov detector to aid particle identification, and a CsI calorimeter for detection of electromagnetic showers. These components are immersed in a magnetic field of 1 T, provided by a superconducting solenoid, and surrounded by a muon detector. The CLEO-c detector is described in detail elsewhere [10].

We reconstruct the $D^+ \to K^-\pi^+\pi^+$ decay using three tracks measured in the tracking system. Charged tracks satisfy standard goodness of fit quality requirements [14]. Pion and kaon candidates are required to have specific ionization, dE/dx, in the main drift chamber within four standard deviations of the expected value at the measured momentum.

In order to select $D^+ \to K^-\pi^+\pi^+$ decays, we use two signal variables,

$$\Delta E = E_D - E_{\text{beam}}, \tag{1}$$

$$m_{\text{BC}} = \sqrt{E^2_{\text{beam}} - \text{P}^2_D}, \tag{2}$$

where E_{beam} is the beam energy, and E_D and P_D are the energy and the magnitude of the momentum of the reconstructed D^+ candidate. We require $|\Delta E| < 2\sigma(\Delta E)$, $|m_{\text{BC}} - m_D| < 2\sigma(m_{\text{BC}})$, where the resolutions $\sigma(\Delta E) = 6$ MeV (5.539 ± 0.014 MeV in single Gaussian fit), and $\sigma(m_{\text{BC}}) = 1.5$ MeV$/c^2$ (1.410 ± 0.013 MeV$/c^2$) represent the widths of the signal peak in the 2D-distribution and projections shown in Fig. 1. In case of multiple D-meson candidates per event we select the one with smallest ΔE value.

We use a kinematic fit to all 3-track candidates which enforces a common vertex and D^+ mass constraint. We require that all events pass the kinematic fit successfully but do not restrict their χ^2. The kinematic fit-corrected 4-momenta of all 3 particles are used to calculate invariant masses for further Dalitz plot analysis.

After all requirements, we select 140793 candidate events for the Dalitz plot analysis. The fraction of background, $\sim$1.1%, in this sample is estimated from the fits to the m_{BC} and ΔE spectra of Fig. 1. In most fits to the Dalitz plot we constrain the value of the signal fraction, $f_{\text{sig}} = 98.917 \pm 0.013\%$. In cross checks we use a set of sub-samples, splitting the data approximately in half by time of observation, and by sign of D-meson charge. We also consider samples with tight (one standard deviation in m_{BC} and ΔE) and loose (three standard deviation) selection versus standard selection (two standard deviations).

To determine the efficiency we use a signal Monte-Carlo (MC) [15] simulation where one of the charged D mesons decays in the signal mode uniformly in the phase space, while the other D meson decays in all known modes with relevant branching fractions. These underlying events are input to the CLEO-c detector simulation and processed with the CLEO-c reconstruction package. The MC-generated events are required to pass the same selection requirements as data selected in the signal box, as shown in Fig. 1(a).

A shape for the background on the Dalitz plot is estimated using data events from a m_{BC} sideband region, shown by the hatched box in Fig. 1. This box is shifted in ΔE to have the same $K^-\pi^+\pi^+$ invariant mass range as candidates in the signal box. We only consider events from the low mass m_{BC} sideband as the high mass sideband has a significant contribution from signal events due to a "tail" caused by initial state radiation. These are clearly seen in the m_{BC} distribution shown in Fig. 1.

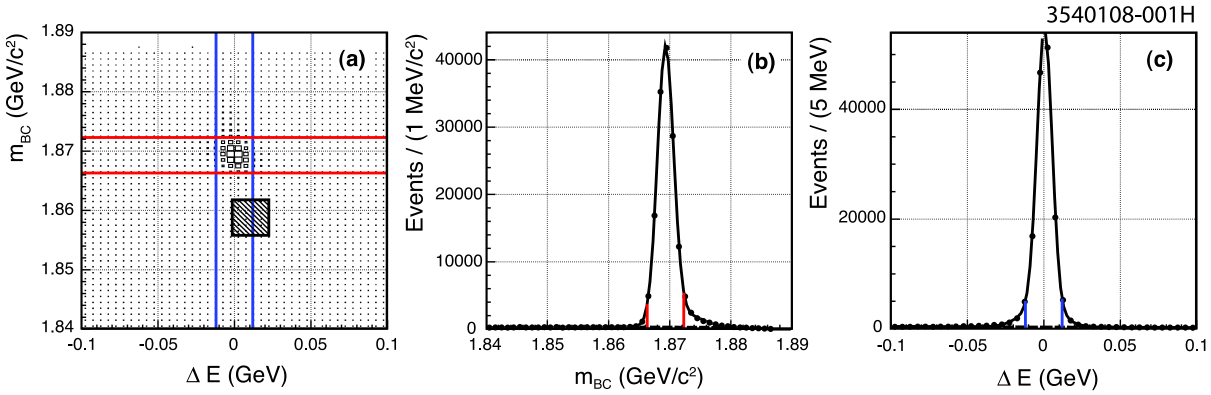

FIG. 1: Event selection, (a) distribution for signal variables $m_{\rm BC}$ *vs.* ΔE. The lines show the $\pm 2\sigma$ bands in ΔE and $m_{\rm BC}$ variables around the signal region. The crossing area of two bands forms the "signal box". The shaded rectangle shows the "background box". Projections after making the $\pm 2\sigma$ selection on the other variable are shown for (b) $m_{\rm BC}$ and (c) ΔE.

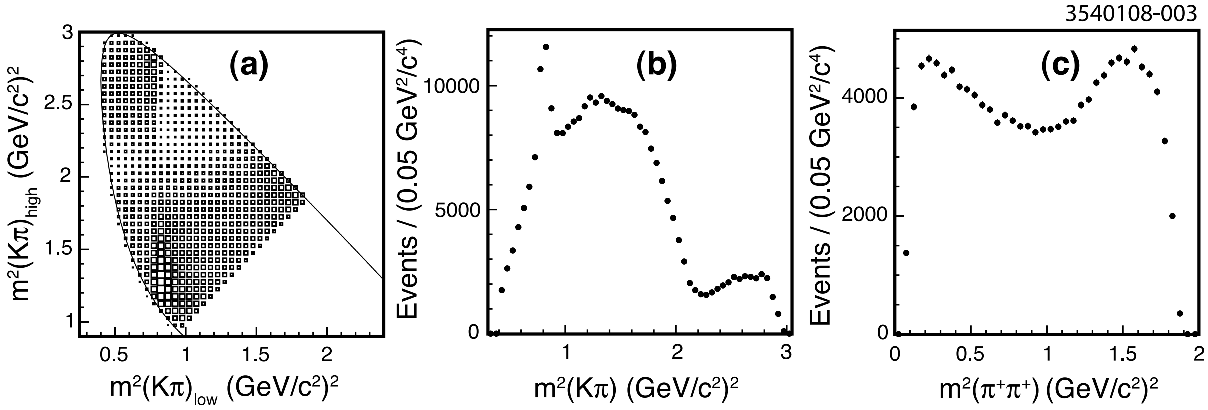

FIG. 2: (a) Dalitz plot for data and its projections on (b) $m^2(K\pi)$ (two entries per event), and (c) $m^2(\pi\pi)$ variables.

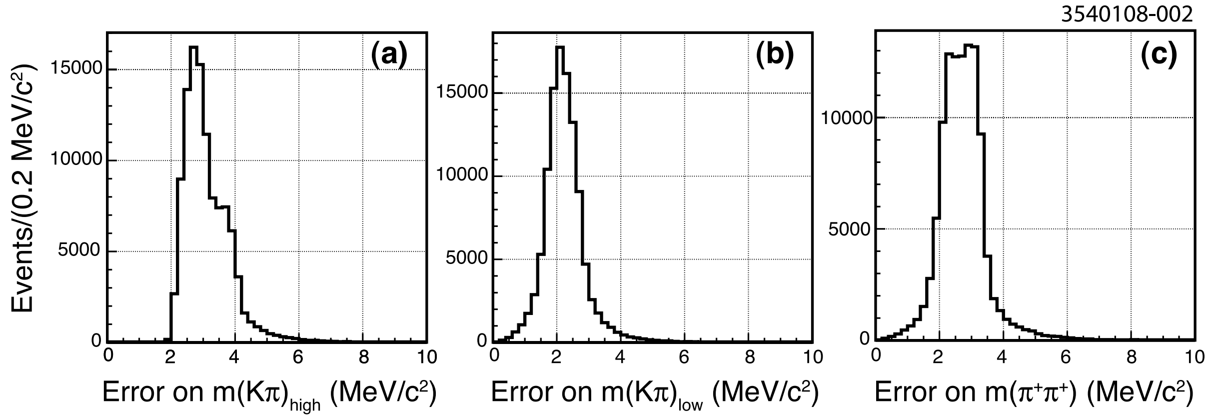

FIG. 3: Invariant mass resolutions for (a) $m(K\pi)_{\rm high}$, (b) $m(K\pi)_{\rm low}$, and (c) $m(\pi\pi)$.

The $K^-\pi^+\pi^+$ final state has two identical π^+ mesons. We account for the Bose symmetry when interchanging the two same-sign charged pions explicitly in our amplitude parameterization. We analyze events on the Dalitz plot by choosing $x = m^2(K^-\pi^+)_{\rm low}$ and $y = m^2(K^-\pi^+)_{\rm high}$ as the independent (x, y) variables. This choice folds all the data onto the top half of the kinematically allowed region, as is shown in Fig. 2(a). The third variable $z \equiv m^2(\pi^+\pi^+)$ is dependent on x and y through energy and momentum conservation. The kinematic fit takes advantage of measurement of all three variables. The invariant mass resolutions before the kinematic fit are shown in Fig. 3. Figure 2 shows data on the Dalitz plot and two projections onto $m^2(K\pi)$ and $m^2(\pi\pi)$ axes. There are two entries per event. Besides the clear $K^*(892)$ signal, no other narrow features are obvious. The strong left-right asymmetry of the $K^*(892)$ population density on the Dalitz plot is evidence of the interference between P and S waves. There are broad structures, including a peak at $m(K\pi)$ around 1.1 GeV/c^2, a dip at $m(K\pi)$ around 1.5 GeV/c^2, a dip at $m(\pi\pi)$ around 1 GeV/c^2, and a peak at $m(\pi\pi)$ around 1.3 GeV/c^2, that do not obviously correspond with known resonances or their reflections from other axes. These structures also do not correspond to a flat phase space distribution for non-resonant decays, since our efficiency is essentially flat across the Dalitz plot, and the background is very low. Thus, we are compelled to consider $K\pi$ strong interaction dynamics to explain the Dalitz plot.

To parameterize the efficiency, $\varepsilon(x, y)$, we use a symmetric third-order polynomial function with respect to the arbitrary point $(x_c,\ y_c)$=(1.5, 1.5) (GeV/c^2)^2 on the Dalitz plot. With $\hat{x} \equiv x - x_c$ and $\hat{y} \equiv y - y_c$, the efficiency is the product of the polynomial function,

$$\varepsilon(x, y) = 1 + E_1(\hat{x} + \hat{y}) + E_2(\hat{x}^2 + \hat{y}^2) + E_3(\hat{x}^3 + \hat{y}^3) + E_{xy}\hat{x}\hat{y} + E_{xyn}(\hat{x}^2\hat{y} + \hat{x}\hat{y}^2), \qquad (3)$$

and sine-like threshold factors for each Dalitz plot variable, v ($\equiv x, y$ or z),

$$T(E_{{\rm th},v}, v_{\rm max}) = \begin{cases} \sin(E_{{\rm th},v} \cdot |v - v_{\rm max}|), & \text{at } 0 < E_{{\rm th},v} \cdot |v - v_{\rm max}| < \pi/2, \\ 1, & \text{at } E_{{\rm th},v} \cdot |v - v_{\rm max}| \geq \pi/2, \end{cases} \qquad (4)$$

where all polynomial coefficients, E_1, E_2, E_3, E_{xy}, E_{xyn}, and $E_{{\rm th},v}$, are the fit parameters. Each variable v has two thresholds, $v_{\rm min}$ and $v_{\rm max}$. But we expect low efficiency in the regions $v \sim v_{\rm max}$ only, where one of three particles is produced with zero momentum in the D meson rest frame and thus has a small momentum in the laboratory frame.

The signal MC sample, with the signal mode decaying uniformly in phase space as described above, is used to determine the efficiency. In each event we only consider the signal mode side to prevent non-uniformity of the efficiency due to the resonance substructure of other side D decay currently implemented in our generic simulation. Figure 4 and Table I show results of the fit to the entire signal MC sample of $D \to K\pi\pi$ events selected on the Dalitz plot. The polynomial function with threshold factors describes the efficiency shape very well for our nominal sample. We also fit separately the signal MC sub-samples for $D^+ \to K^-\pi^+\pi^+$ and $D^- \to K^+\pi^-\pi^-$ decays, for simulations of early and late datasets, and for tight and loose cuts on signal box. In cross-checks with sub-samples we find that the variation of the efficiency parameters is small compared to their statistical uncertainties. In fits with data we use this efficiency shape with fixed parameters, and constrained variation is allowed as a systematic check.

To parametrize the background shape on the Dalitz plot we employ a function similar to that used for the efficiency, shown in Eqs. 3 and 4. We do not apply any peaking contributions due to resonances as the background is a small contribution that has little effect on our fits.

TABLE I: Fit parameters for the efficiency using the signal MC sample.

Parameter	Value
E_1	–0.0153±0.0090
E_2	–0.030±0.011
E_3	0.162±0.020
E_{xy}	–0.053±0.019
E_{xyn}	0.673±0.055
$E_{\mathrm{th},x} \equiv E_{\mathrm{th},y}$	4.25±0.23
$E_{\mathrm{th},z}$	2.907±0.075
Pearson χ^2/ν	649/573
Probability (%)	1.5
Events on DP	477978

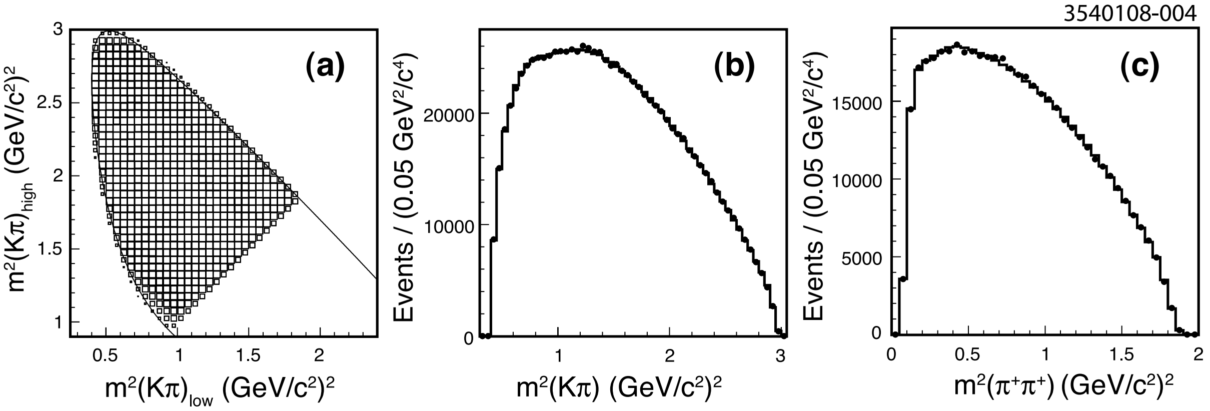

FIG. 4: Fit to the efficiency shape: (a) density distribution of simulated events on the Dalitz plot and its projections on (b) $m^2(K\pi)$ (two entries per event), and (c) $m^2(\pi\pi)$ variables. The solid histogram is a projection of the fitted function.

The pile-up of events at high $K\pi$ invariant mass is caused by combinatorial background, and is observed in our simulation. Figure 5 and Table II show results of the fit to the background polynomial function for our nominal sample. We also consider the variation of the background shape parameters for sub-samples, split for D^+ and D^-, for earlier and later datasets, and for tight and loose selection requirements on the background selection box. The variation of the shape parameters is small compared to their statistical uncertainties. Furthermore, in fits with data, we use the nominal background shape with fixed parameters, and constrained variation is allowed as a systematic cross check.

TABLE II: Fit parameters for the background.

Parameter	Nominal value
B_1	0.63±0.22
B_2	0.95±0.39
B_3	0.41±0.54
B_{xy}	–0.20±0.62
B_{xyn}	–1.2±1.3
$B_{thXYmax}$	1.31±0.13
B_{thZmax}	11.2±6.5
Pearson χ^2/ν	129 / 97
Probability (%)	1.6
Events on DP	1554

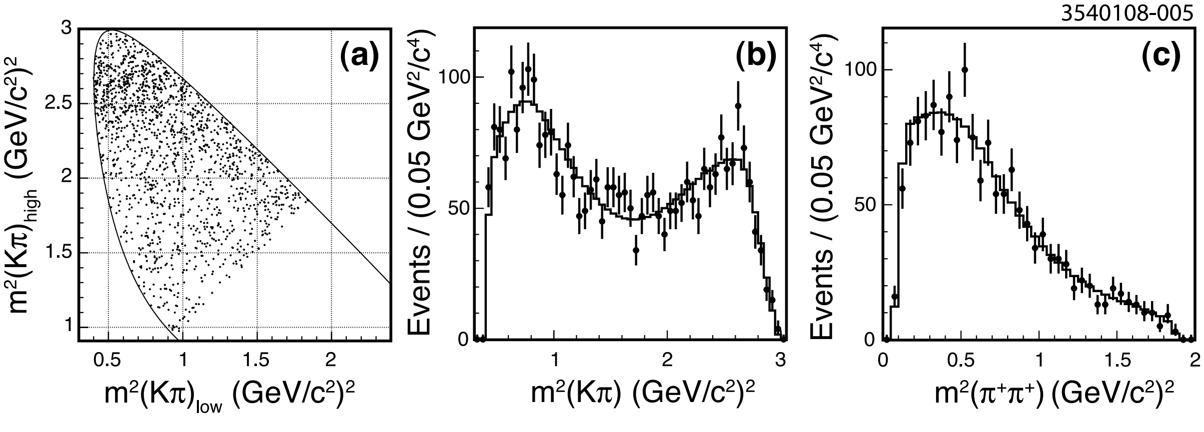

FIG. 5: Fit to the background shape, (a) distribution of events from the background box on the Dalitz plot and its projections on (b) $m^2(K\pi)$ (two entries per event), and (c) $m^2(\pi\pi)$ variables. The solid histogram shows the projection of the fitted function.

III. DECAY AMPLITUDE PARAMETERIZATION

In this analysis we follow the formalism of E791 [6] with only minor variations. In the formulas below for the Dalitz plot variables, we also use Mandelstam notations, $s = m^2(K^-\pi_1^+)$, $t = m^2(K^-\pi_2^+)$, and $u = m^2(\pi_1^+\pi_2^+)$. We choose two of them, s and t, as independent and the third, u, the dependent variable is constrained by the equation $s+t+u = m_D^2 + m_K^2 + 2m_\pi^2$. Then, the matrix element has an explicit Bose-symmetric form for pion permutations

$$\mathcal{M}(s,t) = A(s,t) + A(t,s) + A_{L=0}^{I=2}(u(s,t)). \tag{5}$$

Each $K\pi$ amplitude is defined using a sum over decay orbital momentum L of two-body partial waves

$$A(s,t) = \sum_{L=0}^{L_{\max}} (-2\mathrm{P}_a\mathrm{P}_c)^L \mathcal{P}_L(\cos\theta)\mathcal{F}_D^L(\mathrm{P}_c^*, r_D)\mathcal{A}_L(s), \tag{6}$$

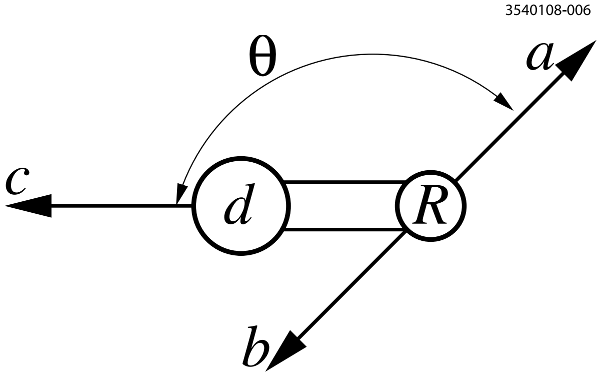

FIG. 6: Three-body decay $d \to Rc \to abc$ in the resonance R rest frame.

with parameters as described below. In this analysis we consider the sum up to the maximal orbital momentum $L_{\rm max} = 2$.

We assume the $D^+ \to K^-\pi^+\pi^+$ decay goes via a quasi-two-body intermediate state, $d \to Rc$, containing the resonance R and particle c, followed by the decay of the resonance to the final stable particles a and b, $R \to ab$. This is shown schematically in Fig. 6. The kinematic variables in Eq. 6 can be expressed in terms of invariant variables (masses and invariant masses) in the decaying particle d (D^+ meson) or resonance R rest frames. The energy and momentum of particle a in the resonance R or (ab) rest frame can be obtained from the 4-momentum balance equation $p_b = p_R - p_a$, where $p_R = (m_{ab}, \vec{0})$, $p_a = (E_a, \mathbf{P}_a)$. Then, $p_b^2 = m_b^2 = m_{ab}^2 + m_a^2 - 2m_{ab}E_a$, giving the energy

$$E_a = \frac{m_{ab}^2 + m_a^2 - m_b^2}{2m_{ab}}, \tag{7}$$

and relevant momentum squared

$$\mathrm{P}_a^2 = E_a^2 - m_a^2 = \frac{1}{4}\Big(m_{ab}^2 - 2m_a^2 - 2m_b^2 + \frac{(m_a^2 - m_b^2)^2}{m_{ab}^2}\Big). \tag{8}$$

The energy and momentum of the particle c in the resonance R rest frame can be obtained from the particle d invariant mass squared, $m_d^2 = (p_c + p_R)^2$. In the resonance rest frame $p_c = (E_c, \mathbf{P}_c)$, $p_R = (m_{ab}, \vec{0})$, and therefore $m_d^2 = m_c^2 + m_{ab}^2 + 2m_{ab}E_c$, from which we find its energy

$$E_c = \frac{m_d^2 - m_{ab}^2 - m_c^2}{2m_{ab}}, \tag{9}$$

and the associated momentum squared

$$\mathrm{P}_c^2 = E_c^2 - m_c^2 = \frac{1}{4}\Big(m_{ab}^2 - 2m_d^2 - 2m_c^2 + \frac{(m_d^2 - m_c^2)^2}{m_{ab}^2}\Big). \tag{10}$$

The energy and momentum of the same particle c in the D meson rest frame, denoted by the asterisk, have different expressions:

$$E_c^* = \frac{m_d^2 - m_{ab}^2 + m_c^2}{2m_d}, \qquad \mathrm{P}_c^{*2} = E_c^{*2} - m_c^2. \tag{11}$$

The angular distributions in Eq. 6 are defined by the Legendre polynomials $\mathcal{P}_L(\cos\theta)$,

$$\mathcal{P}_0(x) = 1, \quad \mathcal{P}_1(x) = x, \quad \mathcal{P}_2(x) = \frac{3x^2 - 1}{2}, \quad \mathcal{P}_3(x) = \frac{5x^3 - 3x}{2}, \ldots, \tag{12}$$

where θ is the angle between particles a and c in the resonance R rest frame. This $\cos\theta$ can be expressed through the known energies and momenta of particles a and c and their measured invariant mass squared $m^2_{ac} = (p_a + p_c)^2 = m^2_a + m^2_c + 2E_aE_c - 2\mathrm{P}_a\mathrm{P}_c\cos\theta$,

$$\cos\theta = \frac{m^2_a + m^2_c + 2E_aE_c - m^2_{ac}}{2\mathrm{P}_a\mathrm{P}_c}. \tag{13}$$

Substituting E_a and E_c from Eqs. 7 and 9 in the numerator of Eq. 13 we get

$$\cos\theta = \frac{1}{4\mathrm{P}_a\mathrm{P}_c}\left(m^2_{bc} - m^2_{ac} + \frac{(m^2_d - m^2_c)(m^2_a - m^2_b)}{m^2_{ab}}\right). \tag{14}$$

Note that these expressions for the angular distributions are equivalent to formulas used in earlier CLEO publications up to a constant factor. Indeed, comparing the angular distributions from Eqs. 6, 7, and 11 in Ref. [16], denoted here as Ω_L, with the expressions for $(-2\mathrm{P}_a\mathrm{P}_c)^L \cdot \mathcal{P}_L(\cos\theta)$ from Eq. 6, we get

$$(-2\mathrm{P}_a\mathrm{P}_c)^0 \cdot \mathcal{P}_0(\cos\theta) = 1 = \Omega_{L=0}, \tag{15}$$

$$(-2\mathrm{P}_a\mathrm{P}_c)^1 \cdot \mathcal{P}_1(\cos\theta) = -2\mathrm{P}_a\mathrm{P}_c\cos\theta = \frac{1}{2}\cdot\Omega_{L=1}, \tag{16}$$

$$(-2\mathrm{P}_a\mathrm{P}_c)^2 \cdot \mathcal{P}_2(\cos\theta) = 4(\mathrm{P}_a\mathrm{P}_c)^2 \cdot \tfrac{3\cos^2\theta - 1}{2} = \frac{3}{8}\cdot\Omega_{L=2}. \tag{17}$$

The form factors $\mathcal{F}^L_D(q)$ in Eq. 6 and $\mathcal{F}^L_R(q)$ in Eqs. 26 and 28 are defined using the Blatt-Weisskopf form [17]

$$L = 0: \quad \mathcal{F}^0_R(q) = 1, \tag{18}$$

$$L = 1: \quad \mathcal{F}^1_R(q) = \mathcal{N}^1_R \cdot (1 + q^2)^{-1/2}, \tag{19}$$

$$L = 2: \quad \mathcal{F}^2_R(q) = \mathcal{N}^2_R \cdot (9 + 3q^2 + q^4)^{-1/2}, \tag{20}$$

where $q = \mathrm{P}\cdot r_R$, P is the decay products' momentum value in the decaying particle rest frame, r_R is an effective resonance radius, and $\mathcal{N}^L_R$ is a normalization constant defined by the condition $\mathcal{F}^L_R(\mathrm{P}_R \cdot r_R) = 1$, where P_R is the momentum value at $m = m_R$. The values of radial parameters are discussed in Sec. IV. We use a constant form factor for scalar resonances in contrast with E791 [6], where a Gaussian form factor,

$$\mathcal{F}^0_R(q) = \mathcal{N}^0_R \cdot e^{-q^2/12}, \tag{21}$$

is applied. The Gaussian form factor shape is suggested by Tornquist [18], and has a steep dependence on momentum which is equivalent to $L = 4$ of the Blatt-Weisskopf form factor [17]. A reanalysis of the E791 data [12] found that this form factor is not required by the data. In our analysis we find that this form factor leads to an artificial rise of the amplitude at low $K\pi$ mass, which looks like a low mass resonance. In our analysis we do not use the form factor for scalar resonances, except when we are comparing results directly with E791. We also do not use form factors with the binned partial waves discussed below.

The partial waves $\mathcal{A}_L(s)$ in Eq. 6 are the angular momentum L-dependent functions of a single variable s or t for $K\pi$ and u for $\pi\pi$. In the $D^+ \to K^-\pi^+\pi^+$ decay the S, P and D waves (L = 0, 1, or 2, respectively) are represented by the sum of wave functions W_R for individual intermediate states

$$
\begin{aligned}
\mathcal{A}_0(s) &= c_{NR} + W_\kappa + W_{K_0^*(1430)} + W_{S,\text{binned}}, &(22)\\
\mathcal{A}_1(s) &= W_{K^*(892)} + W_{K^*(1410)} + W_{K^*(1680)} + W_{P,\text{binned}}, &(23)\\
\mathcal{A}_2(s) &= W_{K_2^*(1430)} + W_{D,\text{binned}}, &(24)\\
\mathcal{A}_0^{I=2}(u) &= W_S^{I=2} + W_{S,\text{binned}}^{I=2}, &(25)
\end{aligned}
$$

where

$$W_R = c_R \cdot \mathcal{W}_R(s) \cdot \mathcal{F}_R^L(\mathrm{P}_a \cdot r_R) \tag{26}$$

is the shape of an individual resonance, $\mathcal{W}_R(s)$ (see Eqs. 27–30), multiplied by the form factor in the resonance R decay vertex, $\mathcal{F}_R^L(\mathrm{P}_a \cdot r_R)$, and the coupling constant, $c_R = a_R e^{i\phi_R}$. The resonance R production magnitudes, a_R, and phases, ϕ_R, are parameters of the fit to the Dalitz plot.

For the intermediate resonances $K^*(892)$, $K^*(1410)$, $K_2^*(1430)$, and $K^*(1680)$ we use the standard Breit-Wigner function,

$$\mathcal{W}_R(m) = \frac{1}{m_R^2 - m^2 - i m_R \Gamma(m)}, \tag{27}$$

where $m^2 = s$, and the mass-dependent width has the usual form

$$\Gamma(m) = \Gamma_R \frac{m_R}{m} \left(\frac{\mathrm{P}}{\mathrm{P}_R}\right)^{2L+1} [\mathcal{F}_R^L(\mathrm{P} \cdot r_R)]^2. \tag{28}$$

For $K_0^*(1430)$ we have tested both the Breit-Wigner function, Eq. 27, and the Flatté parameterization,

$$\mathcal{W}_R(m) = \frac{1}{m_R^2 - m^2 - i \sum_{ab} g_{Rab}^2 \rho_{ab}(m)}, \tag{29}$$

where g_{Rab} is a coupling constant of resonance R to the final state ab, and $\rho_{ab}(m) = 2\mathrm{P}_a/m$ is a phase space factor. We use the Flatté parameterization because the $K_0^*(1430)$ mass is close to the $K\eta$ and $K\eta'$ thresholds, which could significantly distort the resonance shape [12].

For a low invariant mass $K\pi$ S wave we tested the Breit-Wigner function, following E791, and the complex pole proposed in Ref. [13],

$$\mathcal{W}_R(m) = \frac{1}{s_R - m^2}, \tag{30}$$

where s_R is a pole position in the complex $s = m^2$ plane. This function represents the first term of the Laurent series in the expansion of the chiral perturbation theory complex amplitude for the scalar wave discussed in Ref. [13]. In particular, the suggestion is to use the pole $s_\kappa = (0.71 - i0.31)^2$ GeV^2 for the low mass $K\pi$ S wave, to correctly account for the phase of the complex scattering amplitude. This approach is common, and a survey of pole positions extracted from different experiments can also be found in Ref. [11]. This complex pole is equivalent to a Breit-Wigner function with constant width.

The isospin-two $\pi^+\pi^+$ S-wave amplitude $A^{I=2}_{L=0}(u)$ in Eq. 5 is parametrized by a unitary form [19],

$$\mathcal{W}^{I=2}_{L=0}(m) = \frac{\eta^2_0(m)e^{i\delta^2_0(m)} - 1}{2i}, \tag{31}$$

where m is a $\pi^+\pi^+$ invariant mass, $\eta^2_0(m)$ is an inelasticity, and $\delta^2_0(m)$ is a phase of the $\pi^+\pi^+$ scattering.

The phase $\delta^2_0(m)$ is assumed to be proportional to the decay momentum at threshold and sculpted by a polynomial function at higher mass range,

$$\delta^2_0(m) = \frac{-a\sqrt{m^2/4 - m^2_\pi}}{1 + bm^2 + cm^4 + dm^6}. \tag{32}$$

with parameters $a = (55.21 \pm 3.18)$ deg/GeV, $b = (0.853 \pm 0.254)$ GeV^{-2}, $c = (-0.959 \pm 0.247)$ GeV^{-4}, and $d = (0.314 \pm 0.070)$ GeV^{-6}, obtained in Ref. [19] from a fit to data of the scattering experiments [9]. We use this function with fixed parameters.

The parameter $\eta^2_0(m)$ is the inelasticity of the wave with total spin 0 and isospin-two. In the mass range of $m < m(\rho\rho)$ ($\sim$1.54 GeV) the inelasticity parameter $\eta^2_0(m)$ is expected to be near unity. Rescattering to other modes is expected due to the two-ρ re-scattering at a higher mass range. A qualitative fit to data has been considered in Ref. [20] (see Fig. 2). In our fits we use the approximation

$$\eta^2_0(m) = \begin{cases} 1, & m \leq m_{\min} \sim 1 \text{ GeV}/c^2 \\ 1 - \frac{\Delta\eta}{2}\left[1 - \cos\left(\pi \cdot \frac{m - m_{\min}}{m_{\max} - m_{\min}}\right)\right], & m_{\min} < m < m_{\max} \\ 1 - \Delta\eta, & m \geq m_{\max} \sim 1.7 \text{ GeV}/c^2, \end{cases} \tag{33}$$

with fit parameters, $m_{\min}$, $m_{\max}$, and $\Delta\eta$.

The complex term $W_{L,\text{binned}}$ in Eqs. 22-25, where L=0, 1, or 2, is intended to provide a completely model-free parameterization of the partial wave. It can be used alone or in combination with other terms. In the latter case it represents a correction to the complex amplitude of the isobar model. We use this term in the form of an s-dependent complex number

$$W_{L,\text{binned}}(s) = a_{Lk(s)} \cdot e^{i\phi_{Lk(s)}}, \tag{34}$$

defined in bins for the magnitude, $a_{Lk(s)}$, and phase, $\phi_{Lk(s)}$, where $k(s) = 1, 2, \ldots, N_L$ is an s-dependent index of these bins.

For all $K\pi$ waves we define 26 uniform bins in $s \equiv m^2_{K\pi}$ in the range [0.4,3.0] (GeV/c^2)^2, as shown in Table III. For $I = 2$ $\pi^+\pi^+$ S wave we define 18 uniform bins in $u \equiv m^2_{\pi\pi}$ in the range [0.1,1.9] (GeV/c^2)^2, listed in Table IV. This binning scheme covers the kinematically allowed range of the $K\pi$ and $\pi^+\pi^+$ invariant mass spectrum in the $D^+ \to K^-\pi^+\pi^+$ decay. We linearly interpolate between bin centers in our fitting function.

A priori, all known $K\pi$ resonances in the mass range from the production threshold up to $\sim$ 1.73 GeV/c^2, such as $K^*(892)$, $K^*(1410)$, $K^*_0(1430)$, $K^*_2(1430)$, $K^*(1680)$, and even higher mass resonances, might contribute to the amplitude of the $D^+ \to K^-\pi^+\pi^+$ decay. Table VI shows parameters of $K\pi$ resonances which have been considered in this analysis. One would also expect an $I = 2$ $\pi^+\pi^+$ S-wave final state interaction. Some of the expected contributions on the Dalitz plot are shown in Fig. 7. In contrast to data, the $K^*(892)$ population density in Fig. 7(b) is symmetric without interference with S wave.

TABLE III: Bins for the $K\pi$ S, P, and D waves and Blatt-Weisskopf form factors for a few resonances in the D-meson decay vertex.

Bin	$m^2_{K\pi}$ $(\mathrm{GeV}/c^2)^2$	$m_{K\pi}$ (GeV/c^2)		Blatt-W. form factors $\mathcal{F}^L_D(m)$ for			Gaussian f.f.
#	Bin range	Bin range	Center	$K^*(892)$	$K^*(1680)$	$K^*_2(1430)$	$K^*_0(1430)$
1	0.4 — 0.5	0.632 — 0.707	0.671	0.888	0.250	0.305	0.347
2	0.5 — 0.6	0.707 — 0.775	0.742	0.918	0.259	0.324	0.380
3	0.6 — 0.7	0.775 — 0.837	0.806	0.948	0.267	0.345	0.415
4	0.7 — 0.8	0.837 — 0.894	0.866	0.982	0.277	0.368	0.451
5	0.8 — 0.9	0.894 — 0.949	0.922	1.017	0.287	0.394	0.489
6	0.9 — 1.0	0.949 — 1.000	0.975	1.055	0.297	0.421	0.528
7	1.0 — 1.1	1.000 — 1.049	1.025	1.096	0.309	0.452	0.570
8	1.1 — 1.2	1.049 — 1.095	1.072	1.140	0.321	0.485	0.612
9	1.2 — 1.3	1.095 — 1.140	1.118	1.188	0.335	0.523	0.656
10	1.3 — 1.4	1.140 — 1.183	1.162	1.240	0.349	0.564	0.700
11	1.4 — 1.5	1.183 — 1.225	1.204	1.296	0.365	0.609	0.746
12	1.5 — 1.6	1.225 — 1.265	1.245	1.358	0.383	0.659	0.792
13	1.6 — 1.7	1.265 — 1.304	1.285	1.425	0.402	0.715	0.839
14	1.7 — 1.8	1.304 — 1.342	1.323	1.499	0.423	0.776	0.885
15	1.8 — 1.9	1.342 — 1.378	1.360	1.581	0.446	0.844	0.932
16	1.9 — 2.0	1.378 — 1.414	1.396	1.672	0.471	0.918	0.978
17	2.0 — 2.1	1.414 — 1.449	1.432	1.773	0.500	0.999	1.023
18	2.1 — 2.2	1.449 — 1.483	1.466	1.886	0.532	1.085	1.067
19	2.2 — 2.3	1.483 — 1.517	1.500	2.013	0.568	1.178	1.109
20	2.3 — 2.4	1.517 — 1.549	1.533	2.157	0.608	1.275	1.150
21	2.4 — 2.5	1.549 — 1.581	1.565	2.320	0.654	1.374	1.189
22	2.5 — 2.6	1.581 — 1.612	1.597	2.506	0.707	1.472	1.226
23	2.6 — 2.7	1.612 — 1.643	1.628	2.719	0.766	1.568	1.259
24	2.7 — 2.8	1.643 — 1.673	1.658	2.962	0.835	1.657	1.290
25	2.8 — 2.9	1.673 — 1.703	1.688	3.240	0.913	1.737	1.318
26	2.9 — 3.0	1.703 — 1.732	1.718	3.554	1.002	1.805	1.342
$m_{K\pi,\ \mathrm{min}} = m_{K^-} + m_{\pi^+} = 0.633\ \mathrm{GeV}/c^2$							
$m_{K\pi,\ \mathrm{max}} = m_{D^+} - m_{\pi^+} = 1.730\ \mathrm{GeV}/c^2$							

IV. FITS TO DATA USING ISOBAR MODEL

First we compare our results, obtained in the framework of the isobar model (IM), with E791 Models A, B, and C from Ref. [5]. In particular, the most complete Model C contains $\bar{K}^*(892)\pi^+$, $\bar{K}^*_0(1430)\pi^+$, $\bar{K}^*(1680)\pi^+$, $\bar{K}^*_2(1430)\pi^+$, $\bar{K}^*(1680)\pi^+$, $\kappa\pi^+$, and non-resonant (NR) contributions. Following E791 we allow an additional scalar $K\pi$ amplitude, the "κ", as a Breit-Wigner with mass-dependent width. Gaussian form factors are used for $K^*_0(1430)$ and κ. For all $K\pi$ resonances with non-zero spin, the radii in the Blatt-Weisskopf [17] form factors, $r_D = 5\ \mathrm{GeV}^{-1}$ and $r_R = 1.5\ \mathrm{GeV}^{-1}$, are fixed to the values used in E791. Statistics and p.d.f. for this model on the Dalitz plot are shown in Fig. 8. The Dalitz plot projections

TABLE IV: Bins for the $I = 2$ $\pi^+\pi^+$ S wave.

Bin #	$m^2_{\pi\pi}$ $(\mathrm{GeV}/c^2)^2$ Bin range	$m_{\pi\pi}$ (GeV/c^2) Bin range	Center
1	0.1 — 0.2	0.316 — 0.447	0.387
2	0.2 — 0.3	0.447 — 0.548	0.500
3	0.3 — 0.4	0.548 — 0.632	0.592
4	0.4 — 0.5	0.632 — 0.707	0.671
5	0.5 — 0.6	0.707 — 0.775	0.742
6	0.6 — 0.7	0.775 — 0.837	0.806
7	0.7 — 0.8	0.837 — 0.894	0.866
8	0.8 — 0.9	0.894 — 0.949	0.922
9	0.9 — 1.0	0.949 — 1.000	0.975
10	1.0 — 1.1	1.000 — 1.049	1.025
11	1.1 — 1.2	1.049 — 1.095	1.072
12	1.2 — 1.3	1.095 — 1.140	1.118
13	1.3 — 1.4	1.140 — 1.183	1.162
14	1.4 — 1.5	1.183 — 1.225	1.204
15	1.5 — 1.6	1.225 — 1.265	1.245
16	1.6 — 1.7	1.265 — 1.304	1.285
17	1.7 — 1.8	1.304 — 1.342	1.323
18	1.8 — 1.9	1.342 — 1.378	1.360
$m_{\pi^+\pi^+,\ \mathrm{min}} = m_{\pi^+} + m_{\pi^+} = 0.279\ \mathrm{GeV}/c^2$			
$m_{\pi^+\pi^+,\ \mathrm{max}} = m_{D^+} - m_{K^-} = 1.376\ \mathrm{GeV}/c^2$			

with p.d.f. components are shown in Fig. 9. Fit fractions and phases, obtained in our fit, are compared with E791 in Table V. Magnitudes are not comparable because of a different choice for normalization. We find a poor fit quality χ^2/ν=531/391 using this model. The NR fit fraction is ∼9%; and the $\kappa\pi$ fit fraction is dominant, ∼33%. For the $K_0^*(1430)$ resonance we measure $m_{K_0^*(1430)} = 1463.0 \pm 0.7 \pm 2.4$ MeV/c^2 and $\Gamma_{K_0^*(1430)} = 163.8 \pm 2.7 \pm 3.1$ MeV/c^2, which are consistent with E791 results, but inconsistent with current PDG [8] values, as shown in Table VI. Similar behavior is reported in a recent preprint [21] from the FOCUS Collaboration. We also measure the κ resonance parameters, $m_\kappa = 809 \pm 1 \pm 13$ MeV/c^2, and $\Gamma_\kappa = 470 \pm 9 \pm 15$ MeV/c^2.

This model reproduces the behavior reported by E791 [5]. Our results for phases, fit fractions, and resonance parameters are statistically consistent with theirs. However the poor fit quality motivates us to explore alternative models of the decay amplitude.

The Gaussian form factors, given by Eq. 21 for scalar resonances, $\mathcal{F}_R^0(\mathrm{P}_c \cdot r_R)$, and $\mathcal{F}_D^0(\mathrm{P}_c^* \cdot r_D)$, behave similar to $L = 4$ Blatt-Weisskopf form factor. This behavior is not preferred by either our or E791 data; see Ref. [12] for details. For all the fits below we do not use form factors for S-wave contributions, assuming that $\mathcal{F}_R^0(\mathrm{P}_c \cdot r_R) = 1$, and $\mathcal{F}_D^0(\mathrm{P}_c^* \cdot r_D) = 1$. With our data we find that results are not very dependent on the assumed resonance decay vertex form factor $\mathcal{F}_R^0(\mathrm{P}_c \cdot r_R)$. However, the D meson decay vertex form factor, $\mathcal{F}_D^0(\mathrm{P}_c^* \cdot r_D)$, changes the amplitude dependence on s significantly. In particular, it suppresses the low $K\pi$ mass

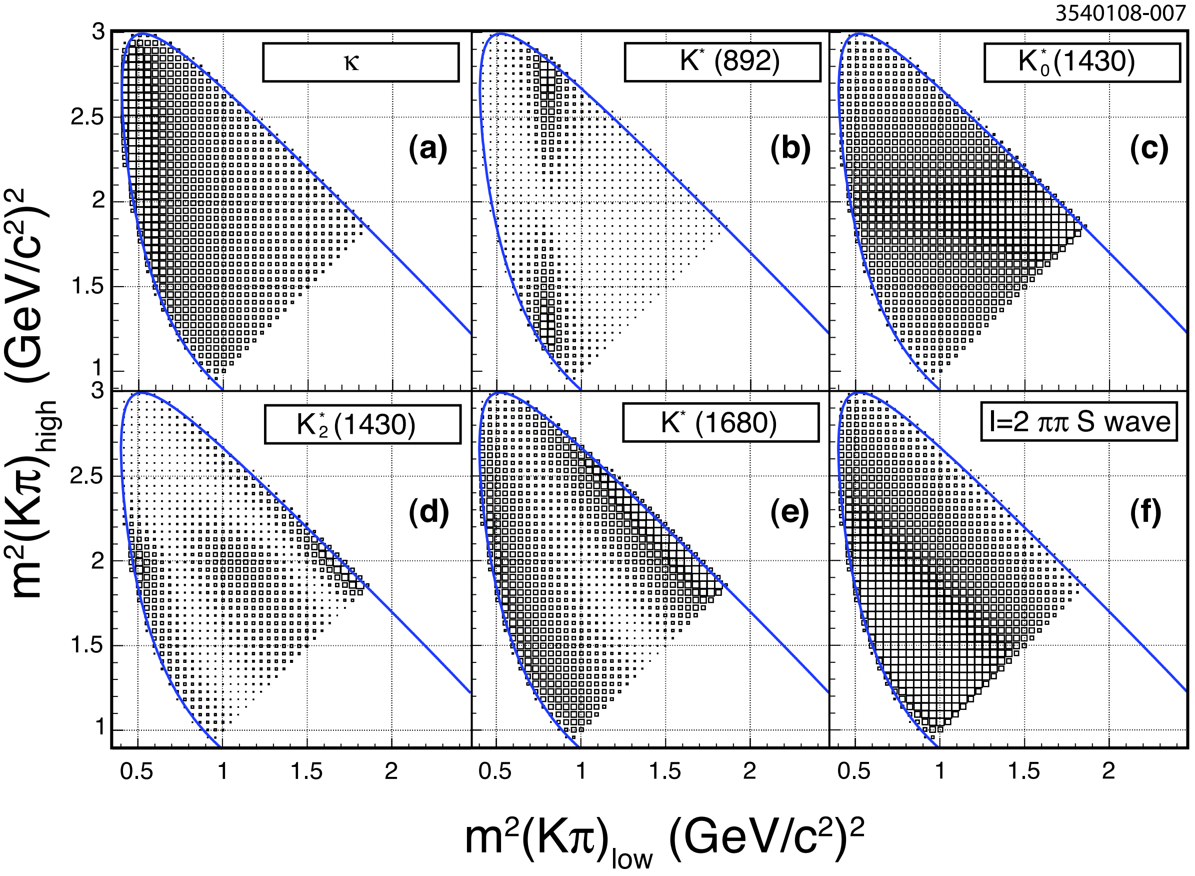

FIG. 7: Expected contribution to the $D^+ \to K^-\pi^+\pi^+$ Dalitz plot from various intermediate states, (a) low mass $K\pi$ S wave (κ), (b) $K^*(892)\pi$, (c) $K_0^*(1430)\pi$, (d) $K_2^*(1430)\pi$, (e) $K^*(1680)\pi$, and (f) $K(\pi\pi)_{I=2}$ with $I = 2$ $\pi^+\pi^+$ S wave.

amplitude. To agree with the data when fitting with this form factor, the magnitude of the complex amplitude increases at low $K\pi$ mass which gives an illusion of resonance behavior. The mass dependence of $\mathcal{F}_D$ form factors for $K\pi$ resonances are shown in Table III.

The optimal mass and width of the $K_0^*(1430)$ resonance are not consistent with PDG [8] values, as shown in Table VI. In Ref. [12] Bugg surmises that the $K_0^*(1430)$ resonance parameters might change due to the opening of the $K\eta'$ channel. In order to accommodate this effect, we test the Flatté parameterization of Eq. 29, which depends on a floating mass, $m_{K_0^*(1430)}$, and three coupling constants, $g_{K\pi}$, $g_{K\eta}$, and $g_{K\eta'}$. We find that our data are consistent with $g_{K\eta} = 0$ and this coupling is dropped from further consideration. The resulting values of the other parameters are shown in Table VII. We do not find any significant difference between Breit-Wigner and Flatté parameterizations in the shape of the $K_0^*(1430)$ complex amplitude, or in the fit quality. We therefore use the Breit-Wigner function for further fits with the mass and width of $K_0^*(1430)$ allowed to float.

In Ref. [13] Oller emphasizes that the Breit-Wigner with mass-dependent width is not the best choice for the $K\pi$ low-mass phase parameterization. Following his prescription, we replace the Breit-Wigner function by the complex pole in Eq. 30, with initial pole position at $s_\kappa = (0.71 - i0.31)^2$ GeV^2. We allow the pole position to float and obtain its optimal location, as shown in Table VII. We find that the pole amplitude slightly improves the fit

TABLE V: Comparison of CLEO-c results with E791 using the isobar fit, Model C. Shown are the fitted magnitudes, a in arbitrary units, the phases, ϕ in degree, defined relative to the $K^*(892)\pi^+$ amplitude, and the fit fractions (FF). Also indicated are the fitted masses, m, and widths, Γ, of the spin-zero resonances. Magnitudes are not comparable because of a different choice for normalization.

Mode	Parameter	E791	CLEO-c
NR	a	1.03±0.30±0.16	7.4±0.1±0.6
	ϕ (°)	–11±14±8	–18.4±0.5±8.0
	FF (%)	13.0±5.8±4.4	8.9±0.3±1.4
$\overline{K}^*(892)\pi^+$	a	1 (fixed)	1 (fixed)
	ϕ (°)	0 (fixed)	0 (fixed)
	FF (%)	12.3±1.0±0.9	11.2±0.2±2.0
$\overline{K}_0^*(1430)\pi^+$	a	1.01±0.10±0.08	3.00±0.06±0.14
	ϕ (°)	48±7±10	49.7±0.5±2.9
	FF (%)	12.5±1.4±0.5	10.4±0.6±0.5
	m (MeV/c^2)	1459±7±12	1463.0±0.7±2.4
	Γ (MeV/c^2)	175±12±12	163.8±2.7±3.1
$\overline{K}_2^*(1430)\pi^+$	a	0.20±0.05±0.04	0.962±0.026±0.050
	ϕ (°)	–54±8±7	–29.9±2.5±2.8
	FF (%)	0.5±0.1±0.2	0.38±0.02±0.03
$\overline{K}^*(1680)\pi^+$	a	0.45±0.16±0.02	6.5±0.1±1.5
	ϕ (°)	28±13±15	29.0±0.7±4.6
	FF (%)	2.5±0.7±0.3	1.28±0.04±0.28
$\kappa\pi^+$	a	1.97±0.35±0.11	5.01±0.04±0.27
	ϕ (°)	–173±8±18	–163.7±0.4±5.8
	FF (%)	47.8±12.1±5.3	33.2±0.4±2.4
	m (MeV/c^2)	797±19±43	809±1±13
	Γ (MeV/c^2)	410±43±87	470±9±15
Form factor	r_κ(GeV^{-1})	1.6±1.3	1.5(fixed)
	r_D(GeV^{-1})	5.0±0.5	5 (fixed)
Other $R \to K\pi$	r_R(GeV^{-1})	1.5(fixed)	1.5(fixed)
$\sum$ FF (%)		88.6	65.5
Goodness	χ^2/ν	46/63	531/391

quality ($\Delta\chi^2 = -12$) compared to the Breit-Wigner with mass-dependent width. We note that this substitution leads to a significant re-distribution of components of the scalar wave. In further fits we use the pole amplitude for the $K\pi$ low-mass S wave.

We also test the $K^*(892)$ parameters, as shown in Table VI. The $K^*(892)$ mass is consistent with the PDG [8] value, while the width is about 5 MeV/c^2 smaller in all our fits. In further analysis we allow the $K^*(892)$ mass and width to float.

Tuning of the isobar model for $K\pi$ waves only does not improve significantly the probability of consistency between the data and the model, which is still small. The largest discrepancy is seen by eye in Fig. 9 for the $m^2(\pi^+\pi^+)$ projection in the range of [1.3, 1.9]

TABLE VI: Optimal Breit-Wigner parameters in the isobar model for $K^*(892)$, κ, and $K_0^*(1430)$: CLEO-c vs E791. The fixed parameters used in the E791 experiment are taken from PDG-2000 with their uncertainties shown in parentheses.

Parameter	E791 (PDG 2000)	CLEO-c		PDG 2006
(MeV/c^2)	Model C (if float)		Model I2 (if float)	
$m_{K^*(892)}$	896.1 (±0.27) fixed	896 (894.8±0.5)	895.7±0.2±0.3	896.00±0.25
$\Gamma_{K^*(892)}$	50.7 (±0.6) fixed	50.3(45.5±0.4)	45.3±0.5±0.6	50.3±0.6
$m_{K_0^*(1430)}$	1459±7±12	1463.0±0.7±2.4	1466.6±0.7±3.4	1414±6
$\Gamma_{K_0^*(1430)}$	175±12±12	163.8±2.7±3.1	174.2±1.9±3.2	290±21
$m_{K_2^*(1430)^0}$	1432.4 (±1.3)	1432.4 (1436±11)	1432.4 (1427±7)	1432.4±1.3
$\Gamma_{K_2^*(1430)^0}$	109 (±5)	109 (132±21)	109 (120±13)	109±5
$m_{K^*(1680)}$	1717 (±27)	1717 (1782±41)	1717 (1679±59)	1717±27
$\Gamma_{K^*(1680)}$	322 (±110)	322 (565±131)	322 (446±119)	322±110
$m_{K^*(1410)}$	1414(±15)	1414	1414	1414±15
$\Gamma_{K^*(1410)}$	232(±21)	232	232	232±21
m_κ	797±19±43	809±1±13	Complex pole,	$K_0^*(800)$ is not
Γ_κ	410±43±87	470±9±15	see Table VII	established

TABLE VII: Alternative parameters obtained in the fits with the isobar model.

Mode	Amplitude	Parameter (MeV/c^2)	Model C	Model I2
$\overline{K}_0^*(1430)\pi^+$	Breit-Wigner	$m_{K_0^*(1430)}$	1463.0±0.7±2.4	1466.6±0.7±3.4
		$\Gamma_{K_0^*(1430)}$	163.8±2.7±3.1	174.2±1.9±3.2
	Flatté	$m_{K_0^*(1430)}$	1462.5±3.9	1471.2±0.8
		$g_{K\pi}$	532.9±8.5	546.8±4.2
		$g_{K\eta}$	0	0
		$g_{K\eta'}$	197±106	230±32
$\kappa\pi^+$	Breit-Wigner	m_κ	809±1±13	888±2
		Γ_κ	470±9±15	550±12
	Complex pole	$\Re m_\kappa$	769.9±6.3	706.0±1.8±22.8
		$\Im m_\kappa$	–221.2±8.4	–319.4±2.2±20.2

(GeV/c^2)^2, where the fit differs from the data. This problem persists even if we use the model independent parameterization for the $K\pi$ S wave considered below. The most natural way to solve this problem is to include a contribution from the $I = 2$ $\pi^+\pi^+$ S wave, using Eq. 31. We include this amplitude in the matrix element, as shown in Eq. 5, without form factors. In this model the inelasticity parameter η_0^2 is equal to one for the mass range below the smooth $\rho\rho$ production threshold. Then η_0^2 decreases due to the $\pi^+\pi^+$ transition into other modes. This threshold is located at the upper edge of the $m^2(\pi^+\pi^+)$ kinematic limit in our decay. The edge of the kinematic border does not allow us to resolve correlations between the $\Delta\eta$ and $m_{\max}$ parameters in Eq. 33. In the next fit, Model I2, we include the $I = 2$

$\pi^+\pi^+$ S wave and fix the value of $\Delta\eta = 1$, while floating the $m_{\rm min}$ and $m_{\rm max}$ parameters.

Using Model I2 we find shape parameters as shown in Table VIII, and have a consistency with the data of ∼13%. The total p.d.f. and separate components are shown in the Dalitz plot projections in Fig. 10. The discrepancy in the $m^2(\pi^+\pi^+)$ spectrum is eliminated. Model I2 is consistent with our data.

TABLE VIII: Fit results for Model I2 and QMIPWA. The fit fractions (FF) are shown for single $K\pi$ wave and need to be doubled as indicated by the "2×" symbol in row-titles.

Mode	Parameter	Model I2 (B-W for κ)	Model I2	QMIPWA
$\overline{K}^*(892)\pi^+$	a	1 – fixed	1 – fixed	1 – fixed
	ϕ (°)	0 – fixed	0 – fixed	0 – fixed
	FF (%) 2×	5.15±0.24	5.27±0.08±0.15	4.94±0.23
	m (MeV/c^2)	895.4±0.2	895.7±0.2±0.3	895.7 – fixed
	Γ (MeV/c^2)	44.5±0.7	45.3±0.5±0.6	45.3 – fixed
$\overline{K}^*(1680)\pi^+$	a	4.45±0.23	3.38±0.16±0.78	2.88±0.84
	ϕ (°)	43.3±3.6	68.2±1.6±13	113±14
	FF (%) 2×	0.238±0.024	0.144±0.013±0.12	0.098±0.059
$\overline{K}^*_2(1430)\pi^+$	a	0.866±0.030	0.915±0.025±0.04	0.794±0.073
	ϕ (°)	–17.4±3.5	–17.4±2.3±2.0	14.8±9.0
	FF (%) 2×	0.124±0.011	0.145±0.009±0.03	0.102±0.020
$\overline{K}^*_0(1430)\pi^+$	a	3.97±0.15	3.74±0.02±0.06	3.74 – fixed
	ϕ (°)	45.1±0.9	51.1±0.3±1.6	51.1 – fixed
	FF (%) 2×	7.53±0.65	7.05±0.14±0.55	6.65±0.31
	m (MeV/c^2)	1461.1±1.0	1466.6±0.7±3.4	1466.6 – fixed
	Γ (MeV/c^2)	177.9±3.1	174.2±1.9±3.2	174.2 – fixed
$\kappa\pi^+$	a	5.69±0.17	10.80±0.05±0.35	0
	ϕ (°)	–149.9±1.2	148.4±0.3±1.6	0
	FF (%) 2×	8.5±0.5	21.6±0.3±3.2	0
pole	$\Re m_0$ (MeV/c^2)		706.0±1.8±22.8	
	$\Im m_0$ (MeV/c^2)		–319.4±2.2±20.2	
Breit-Wigner	m (MeV/c^2)	888.0±1.9		
	Γ (MeV/c^2)	550.4±11.8		
NR	a	17.1±0.4	23.3±0.1±1.6	0
	ϕ (°)	1.9±1.7	29.7±0.2±3.0	0
	FF (%)	38.0±1.9	73.8±0.8±9.6	0
Binned $K^-\pi^+$ S wave	a	0	0	See
	ϕ (°)	0	0	Table IX
	FF (%) 2×	0	0	41.9±1.9
$I = 2$ $\pi^+\pi^+$ S wave	a	30.3±2.7	25.5±0.3±2.9	33.1±2.6
	ϕ (°)	86.3±3.3	75.4±0.6±10	66.2±3.5
	FF (%)	13.4±2.3	9.8±0.2±2.0	15.5±2.8
Eq. 33	$\Delta\eta$	1	1	1
	$m_{\rm min}$ (MeV/c^2)	1265±8	1256±5±4	1256.3 – fixed
	$m_{\rm max}$ (MeV/c^2)	1529±31	1498±13±30	1498.2 – fixed
Form factor	r_D(GeV^{-1})	5 – fixed	5 – fixed	5 – fixed
	r_{Swave}(GeV^{-1})	0 – fixed	0 – fixed	0 – fixed
Other $R \to K\pi$	r_R(GeV^{-1})	1.5 – fixed	1.5 – fixed	1.5 – fixed
	$\sum$ FF$_i$ (%)	94.4	152.0	122.8
Goodness	χ^2/ν	426/385	416/385	359/347
	Probability (%)	7.4%	13.2%	31.5%

V. QUASI-MODEL-INDEPENDENT PARTIAL WAVE ANALYSIS

The biggest issue of any Dalitz plot analysis is its model dependence. An attempt to mitigate the model dependence for the decay under study is described in [6]. Here we reproduce this analysis using a slightly modified technique, which we call the quasi-model-independent partial wave analysis (QMIPWA). We apply this technique as an extension of our Model I2.

We start with the parameters of Model I2 and modify them as follows. The $K\pi$ S wave in Eq. 22 is represented by the binned S-wave amplitude, Eq. 34, instead of the NR and $\kappa\pi$ components. The 26 bins for the S-wave magnitude and the 26 bins for its phase are floating parameters of the fit. We keep the $K_0^*(1430)\pi$ contribution in its Breit-Wigner form, because it has a sharp structure, that cannot be well reproduced by a binned amplitude. The $K_0^*(1430)$ parameters are fixed to their values from Model I2 in order to remove correlations between the Breit-Wigner function and the binned S-wave amplitude. The $K\pi$ P wave in Eq. 23 is represented by the $K^*(892)$ and $K^*(1680)$ Breit-Wigner functions, where the $c_{K^*(1680)}$ parameters are allowed to float in the fit. As usual $c_{K^*(892)} = 1$ and all other magnitudes are defined with respect to $K^*(892)$. In preliminary fits we did not find any significant contribution from $K^*(1410)$ and this resonance is excluded from the P wave. The $K\pi$ D wave in Eq. 24 is represented by the $K_2^*(1430)$ Breit-Wigner function with its parameters, $c_{K_2^*(1430)}$, allowed to float in the fit. The $I = 2$ $\pi^+\pi^+$ S wave is represented by the unitary amplitude from Eq. 31.

The results of this QMIPWA fit are shown in Table VIII for resonance parameters and Table IX for the $K\pi$ S wave. Figure 11 shows the Dalitz plot projections of this fit. The measured $K\pi$ S wave and their comparison with Model I2 components are displayed in Fig. 12. Both the magnitude and phase are different from those of Model I2. Table IX (right-hand side) also shows the result of a similar fit for total binned S wave. For this fit the $K_0^*(1430)$ resonance is accounted for in the binned S wave, and all other parameters are fixed to their values from the previous fit.

In this approach we also check how much the $I = 2$ $\pi^+\pi^+$ S wave might be different from their analytic approximation in the Model I2. We fix all fit parameters to their values in the Model I2 fit except for the 18 magnitude and 18 phase bins for $I = 2$ $\pi^+\pi^+$ S wave which are allowed to float. Results of this fit are shown in Table X. The measured $I = 2$ $\pi^+\pi^+$ S wave is compared to the Model I2 analytic function in Fig. 13. The change of the χ^2 in this fit compared to Model I2, $\Delta\chi^2 = 390 - 416 = -26$ shows a small improvement with the addition of the binned amplitude, but introduces 36 additional degrees of freedom. Our $I = 2$ $\pi^+\pi^+$ S-wave model is consistent with the data.

To check how much the P and D waves might be different from their model parameterization we use the same binned technique. All the fit parameters are fixed to their optimal values from the Model I2. The P-wave binned amplitude substitutes for the smooth $K^*(1680)$ resonance only. The sharp shape of the $K^*(892)$ resonance is accounted for by a Breit-Wigner function. The D-wave binned amplitude substitutes for the $K_2^*(1430)$ contribution, even though it is not particularly smooth. The 26 magnitude and 26 phase bins are allowed to float for each P wave. The resolution for the D wave is worse and we use only 18 bins in the $m^2_{K\pi}$ range [0.9, 2.7] (GeV/c^2)^2. Results of these fits are shown in Table XI. The measured P- and D-binned waves and their comparison with the Model I2 components are displayed in Figs. 14 and 15, respectively.

The relative fraction of P and especially D wave is, not surprisingly, smaller than the S wave. This explains the poor resolution for these binned amplitudes. We find that our binned P and D waves are consistent with their substituted components in the Model I2. This cross-check adds some confidence to this quasi-model-independent technique.

TABLE IX: QMIPWA: Results for $K\pi$ S wave.

Bin	$m^2_{K\pi}$ $(\mathrm{GeV}/c^2)^2$	Binned $K\pi$ S wave w/o $K_0^*(1430)$		Total $K\pi$ S wave	
#	Bin range	Magnitude (a.u.)	Phase (°)	Magnitude (a.u.)	Phase (°)
1	0.4 — 0.5	20.23±0.80±0.51	–71.8±4.9±4.1	19.29±0.56	–66.0±3.2
2	0.5 — 0.6	20.90±0.68±0.54	–61.1±4.6±2.3	20.38±0.51	–54.3±2.8
3	0.6 — 0.7	20.58±0.63±0.69	–48.8±4.0±3.2	20.35±0.45	–40.9±2.2
4	0.7 — 0.8	20.62±0.64±0.51	–47.0±2.4±0.7	20.52±0.59	–39.7±0.9
5	0.8 — 0.9	20.95±0.74±1.32	–44.1±3.6±3.5	20.84±0.49	–36.0±1.4
6	0.9 — 1.0	19.97±0.63±1.14	–38.4±4.0±6.4	19.97±0.36	–28.7±2.7
7	1.0 — 1.1	19.36±0.58±0.96	–26.2±3.5±4.8	19.97±0.34	–15.7±2.6
8	1.1 — 1.2	17.81±0.53±0.96	–18.6±3.0±6.1	18.85±0.30	–6.9±2.0
9	1.2 — 1.3	17.70±0.49±0.90	–13.7±2.6±5.1	19.05±0.27	–1.2±1.6
10	1.3 — 1.4	17.72±0.47±1.05	–8.5±2.5±5.8	19.47±0.25	4.8±1.4
11	1.4 — 1.5	17.13±0.45±1.05	–3.2±2.4±4.7	19.36±0.23	11.6±1.3
12	1.5 — 1.6	17.16±0.45±1.04	0.5±2.3±5.6	19.80±0.22	17.1±1.3
13	1.6 — 1.7	17.09±0.46±1.14	5.4±2.3±4.0	20.35±0.22	24.3±1.3
14	1.7 — 1.8	16.94±0.47±1.06	7.5±2.3±4.6	20.61±0.24	30.1±1.3
15	1.8 — 1.9	16.41±0.48±1.05	9.5±2.4±3.7	20.38±0.27	38.0±1.3
16	1.9 — 2.0	15.91±0.51±0.75	12.3±2.7±3.2	19.86±0.34	49.1±1.4
17	2.0 — 2.1	15.97±0.56±1.11	16.9±2.9±3.1	19.07±0.40	63.4±1.4
18	2.1 — 2.2	15.72±0.61±1.11	15.7±2.5±2.2	14.20±0.40	76.6±1.9
19	2.2 — 2.3	16.54±0.63±1.17	17.3±2.1±2.1	9.29±0.39	75.2±2.6
20	2.3 — 2.4	16.64±0.71±1.42	20.1±2.1±3.4	7.10±0.43	57.5±3.1
21	2.4 — 2.5	15.91±0.86±1.61	19.8±2.3±2.0	6.75±0.43	33.5±3.2
22	2.5 — 2.6	17.25±1.03±1.83	21.5±2.4±2.0	9.46±0.51	26.0±2.5
23	2.6 — 2.7	17.24±1.21±2.38	24.1±2.6±2.9	10.74±0.55	26.7±2.6
24	2.7 — 2.8	17.59±1.34±2.28	29.0±2.8±1.6	12.04±0.64	31.8±2.5
25	2.8 — 2.9	16.51±1.65±2.56	32.7±3.5±3.5	11.79±0.79	36.0±3.3
26	2.9 — 3.0	14.07±3.28±3.32	35.6±6.0±3.8	9.75±2.50	38.6±6.1

VI. SYSTEMATIC UNCERTAINTIES

In order to estimate systematic uncertainties of the fit parameters, we apply numerous variations to the fitting procedure and examine the change of the fit parameters. The *Mean* and *RMS* of all variations are added quadratically to estimate the *Total* uncertainty on each parameter.

Our basic procedure is to consider the six sub-samples, where events are almost evenly split for earlier and later datasets, for D^+ and D^- decays, and are selected using tight $(1\sigma(\Delta E)\times 1\sigma(m_{\mathrm{BC}}))$ and loose $(3\sigma(\Delta E)\times 3\sigma(m_{\mathrm{BC}}))$ cuts on signal box. Depending on the model we apply additional cross checks listed below. The fits marked by "$\circ$" significantly change Model C and bring us to different enough models that we do not include these results in the total systematic uncertainty. We cannot remove the $K_2^*(1430)$ and $K^*(1680)$ resonances. Their contributions are small (FF$<1\%$) but significant and the fit quality is

TABLE X: QMIPWA: Results for $\pi^+\pi^+$ S wave.

Bin #	$m^2_{\pi\pi}$ $(\mathrm{GeV}/c^2)^2$ Bin range	$I=2$ $\pi^+\pi^+$ S wave Magnitude (a.u.)	Phase (°)
1	0.1 — 0.2	3.62±0.44	–113.9±7.0
2	0.2 — 0.3	4.31±0.37	–115.8±4.7
3	0.3 — 0.4	4.51±0.33	–120.7±3.6
4	0.4 — 0.5	6.17±0.33	–116.8±2.4
5	0.5 — 0.6	6.84±0.34	–118.9±2.1
6	0.6 — 0.7	8.13±0.35	–121.8±1.8
7	0.7 — 0.8	7.77±0.35	–121.7±1.9
8	0.8 — 0.9	8.65±0.35	–125.5±1.7
9	0.9 — 1.0	8.95±0.37	–126.3±1.6
10	1.0 — 1.1	9.61±0.42	–127.9±1.5
11	1.1 — 1.2	11.69±0.55	–127.9±1.3
12	1.2 — 1.3	10.04±0.93	–132.0±1.5
13	1.3 — 1.4	12.43±1.01	–131.0±1.2
14	1.4 — 1.5	12.92±0.98	–131.1±1.3
15	1.5 — 1.6	9.51±0.98	–131.4±1.8
16	1.6 — 1.7	11.56±1.00	–134.7±1.8
17	1.7 — 1.8	11.75±1.10	–142.5±2.1
18	1.8 — 1.9	10.52±2.02	–156.1±5.2
	FF(%)	9.8±0.4	
	$\Delta\chi^2(\Delta\nu = 36)$	390 – 416 (in Model I2)	

very poor without these resonances.

For Model C we consider the variants of the fitting procedure as follows.

- We add the $I = 2$ $\pi^+\pi^+$ S wave with fixed shape parameters and find $a_{I=2} = 15.8\pm2.5$, $\phi_{I=2} = 65 \pm 9°$, $FF_{I=2} = 4.6 \pm 1.6\%$. This fit shows that the $I = 2$ $\pi^+\pi^+$ S-wave contribution significantly improves the fit quality of Model C.

- Set to unity the scalar resonance form factors, $\mathcal{F}^0 = 1$, for κ and $K^*_0(1430)$.

- Float the mass and width of $K^*(892)$ and find $m_{K^*(892)} = 894.8 \pm 0.5$ MeV/c^2, $\Gamma_{K^*(892)} = 45.5 \pm 0.4$ MeV/c^2.

- Add a $K^*(1410)$ contribution and find $a_{K^*(1410)} = 0.35 \pm 0.16$, $\phi_{K^*(1410)} = 44 \pm 15°$, $FF_{K^*(1410)} = 0.032 \pm 0.030\%$, or $< 0.1\%$ at 90% C.L.

- Drop the background term and set $f_{\mathrm{sig}} = 1$.

- Float f_{sig} and find $f_{\mathrm{sig}} = 0.9835 \pm 0.0056$. The nominal value is 0.9892.

◦ Set to unity the scalar resonance form factors of the D-meson decay vertex, $\mathcal{F}^0_D = 1$, *i.e.* $r_D = 0$ for κ and $K^*_0(1430)$. This fit shows that $\mathcal{F}^0_D$ form factor for scalar

TABLE XI: : Results for $K\pi$ P- and D-binned waves using the Model I2 described in the text.

Bin #	$m^2_{K\pi}$ (GeV/c^2)^2 Bin range	Binned P wave for $K^*(1680)$ Magnitude (a.u.)	Phase (°)	D-wave corr. to $K_2^*(1430)$ Magnitude (a.u.)	Phase (°)
1	0.4 — 0.5	1.96±1.26	41.0±28.0	0	0
2	0.5 — 0.6	2.90±1.12	199.2±11.2	0	0
3	0.6 — 0.7	0.67±0.93	50.1±15.8	0	0
4	0.7 — 0.8	0.81±0.36	46.4±18.4	0	0
5	0.8 — 0.9	0.60±0.35	102.3±33.7	0	0
6	0.9 — 1.0	0.58±1.36	73.2±25.7	0.71±0.17	–61.8±23.6
7	1.0 — 1.1	1.87±0.77	79.5±7.01	0.31±0.14	–5.0±69.6
8	1.1 — 1.2	0.09±0.42	51.7±22.4	0.66±0.16	–15.6±27.2
9	1.2 — 1.3	1.12±0.38	81.3±10.6	1.14±0.19	–50.0±12.9
10	1.3 — 1.4	1.49±0.33	74.4±8.79	1.09±0.19	–28.7±13.1
11	1.4 — 1.5	0.81±0.33	83.9±13.3	0.97±0.19	–9.9±14.2
12	1.5 — 1.6	1.25±0.33	80.8±10.6	1.30±0.21	–15.5±14.0
13	1.6 — 1.7	1.30±0.34	73.3±9.79	1.45±0.24	11.6±13.5
14	1.7 — 1.8	1.77±0.36	77.7±8.34	2.18±0.26	–16.3±10.2
15	1.8 — 1.9	1.16±0.40	88.1±11.1	3.28±0.28	24.4±7.83
16	1.9 — 2.0	1.79±0.45	90.9±9.91	5.77±0.38	31.9±5.45
17	2.0 — 2.1	1.86±0.42	102.1±11.2	4.77±0.52	70.2±5.90
18	2.1 — 2.2	2.42±0.45	104.3±12.2	4.45±0.70	100.2±7.41
19	2.2 — 2.3	2.58±0.52	115.7±12.6	4.69±0.97	127.8±8.52
20	2.3 — 2.4	1.66±0.55	119.6±16.6	3.79±1.13	116.8±16.3
21	2.4 — 2.5	3.76±0.60	108.8±11.4	0.18±1.42	–3.3±84.7
22	2.5 — 2.6	4.19±0.75	113.6±13.7	4.86±1.72	135.8±33.2
23	2.6 — 2.7	6.71±0.98	105.0±16.9	1.54±2.58	184.8±78.5
24	2.7 — 2.8	3.35±1.59	142.4±29.4	0	0
25	2.8 — 2.9	7.03±2.49	183.2±22.5	0	0
26	2.9 — 3.0	32.66±17.9	232.2±11.6	0	0
FF(%), 2× $\Delta\chi^2(\Delta\nu = 52)$		0.20±0.03 373–416 (in Model I2)		0.15±0.01 400–416 (in Model I2)	

resonances significantly changes the fit parameters. This result is expected due to the strong dependence of this form factor on the $K\pi$ invariant mass, as shown in Table III.

- Use Flatté, rather than Breit-Wigner, for $K_0^*(1430)$. The form factor $\mathcal{F}_D^0$ has a regular $r_D = 5$, and find $m_{K_0^*(1430)} = 1462.5 \pm 3.9$ MeV/c^2, $g_{K\pi} = 532.9 \pm 8.5$ MeV, $g_{K\eta'} = 197 \pm 106$ MeV. This fit shows that both the Breit-Wigner and Flatté shape for $K_0^*(1430)$ are equally good descriptions of the data.

▽ Use a complex pole rather than a Breit-Wigner for the κ. Fix a_{NR} and ϕ_{NR} to their values from Model C. The form factor $\mathcal{F}_D^0$ has a regular $r_D = 5$ and $\Re m_\kappa = 769.9 \pm 6.3$ MeV/c^2, $\Im m_\kappa = -221.2 \pm 8.4$ MeV/c^2.

- ◦ The same as "$\bigtriangledown$", but float NR and find $\Re m_\kappa = 655 \pm 13$ MeV/c^2, $\Im m_\kappa = -231 \pm 14$ MeV/c^2. The last two fits show that the complex pole parameterization for the κ amplitude behaves differently from its Breit-Wigner shape. In particular, the interference with the NR amplitude gives different optimal solutions for the complex pole and Breit-Wigner. The fit parameters of other resonances do not change, but the fit fractions are changed dramatically due to the large variation of NR and κ amplitudes in these two fits.

- ◦ The same as "$\bigtriangledown$", but use a unity form factor for κ, $\mathcal{F}_D^0 = 1$, and find $\Re m_\kappa = 626 \pm 22$ MeV/c^2, $\Im m_\kappa = -222 \pm 17$ MeV/c^2.

- • Float the efficiency coefficients in a simultaneous fit to data and MC samples.

- ◦ Model C for event sample without a kinematic fit with appropriate coefficients for efficiency and background.

- ◦ Remove $K_2^*(1430)$ resonance contribution, $\Delta\chi^2 = 370$.

- ◦ Remove $K^*(1680)$ resonance contribution, $\Delta\chi^2 = 250$.

- • Float mass and width of $K_2^*(1430)$ and find $m_{K_2^*(1430)} = 1436 \pm 11$ MeV/c^2 [1432.4 MeV/c^2 in PDG], $\Gamma_{K_2^*(1430)} = 132 \pm 21$ MeV/c^2 [109 MeV/c^2 in PDG].

- • Float mass and width of $K^*(1680)$ and find $m_{K^*(1680)} = 1782 \pm 41$ MeV/c^2 [1717 MeV/c^2 in PDG], $\Gamma_{K^*(1680)} = 565 \pm 131$ MeV/c^2 [322 MeV/c^2 in PDG].

We apply a similar procedure for the Model I2 and on the model independent S-wave measurement.

- Float parameters of the $K_2^*(1430)$ or $K^*(1680)$ resonances. The mass and width are shown in Table VI.

- Add the $K^*(1410)$ resonance.

- Use the binned $K^-\pi^+$ S wave as a histogram without linear interpolation.

- Remove one by one the $K_2^*(1430)$, $K^*(1680)$ resonances and the $I = 2$ $\pi^+\pi^+$ S-wave contribution.

- Simultaneous fit with efficiency event sample and floating efficiency parameters.

- Improve precision by an order of magnitude of normalization integral calculation.

- Drop the background term, and set $f_{\rm sig} = 1$. The nominal value is $f_{\rm sig} = 0.9892$.

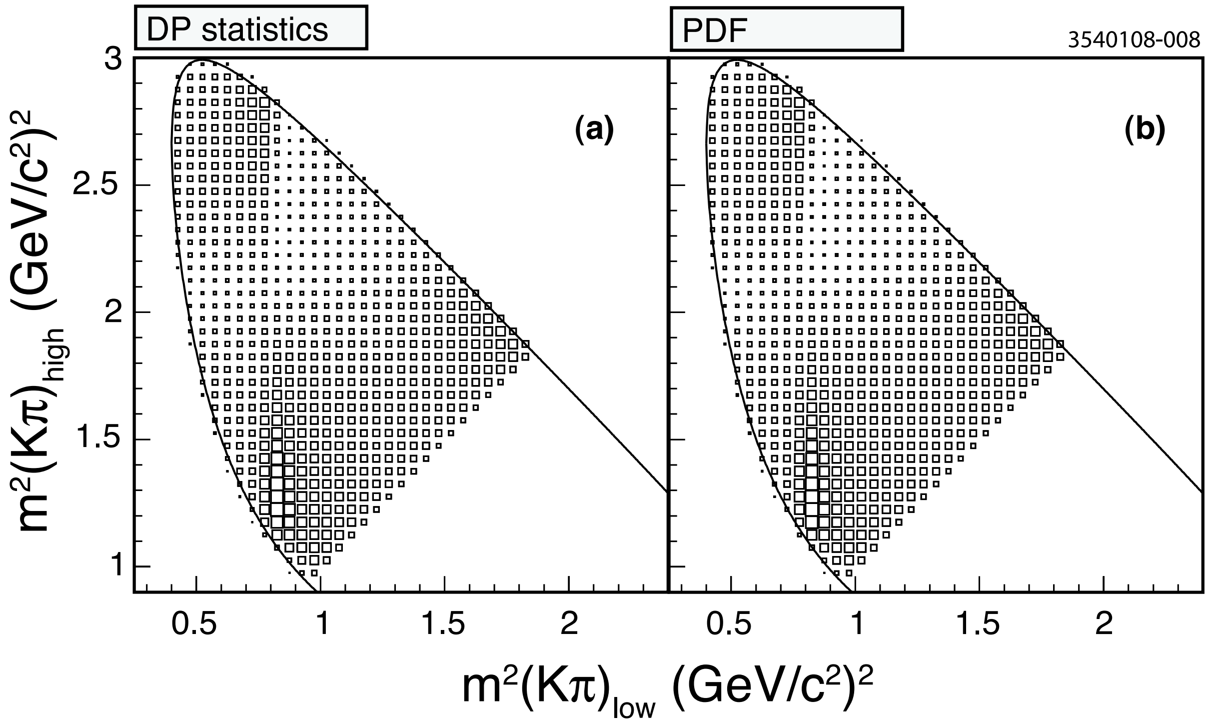

FIG. 8: (a) Statistics and (b) fitted p.d.f. in Model C on the Dalitz plot.

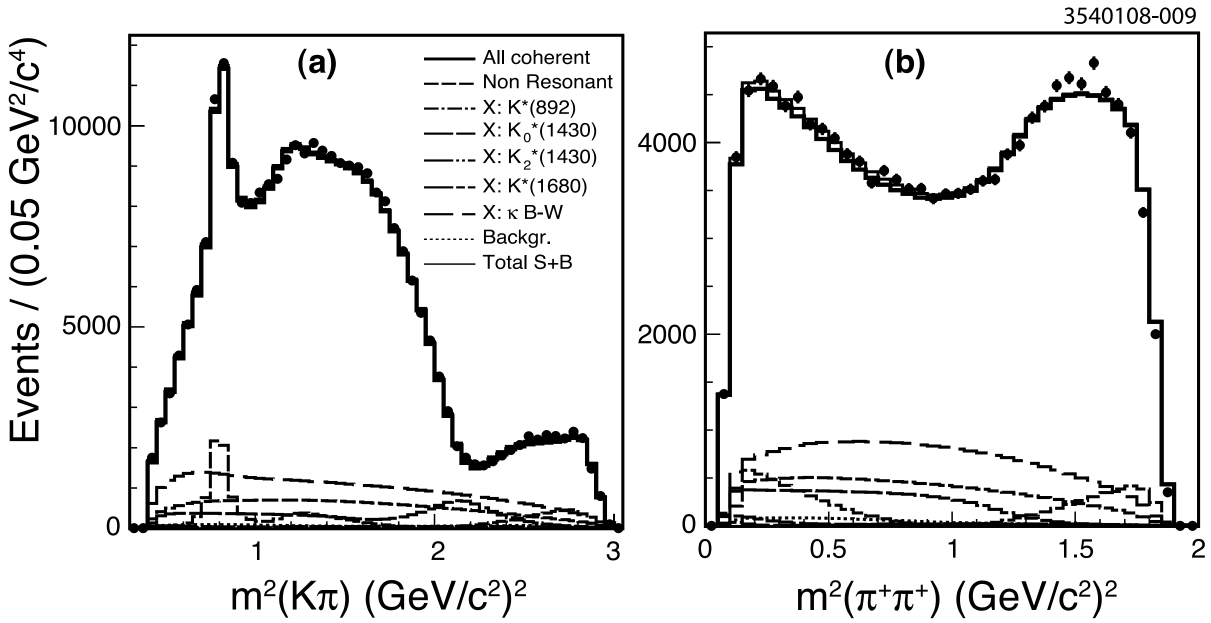

FIG. 9: Projections of the Dalitz plot on (a) $m^2(K\pi)$ (two entries per event), and (b) $m^2(\pi\pi)$ variables; comparison with E791, Model C.

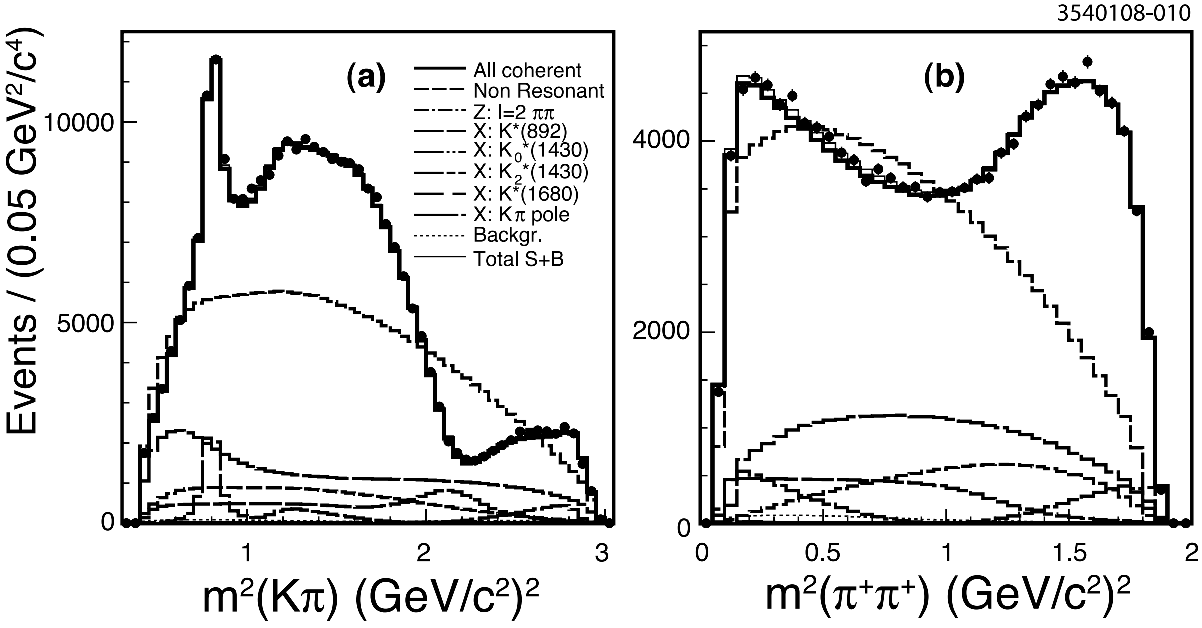

FIG. 10: Projections of the Dalitz plot on (a) $m^2(K\pi)$ (two entries per event), and (b) $m^2(\pi\pi)$ variables for Model I2.

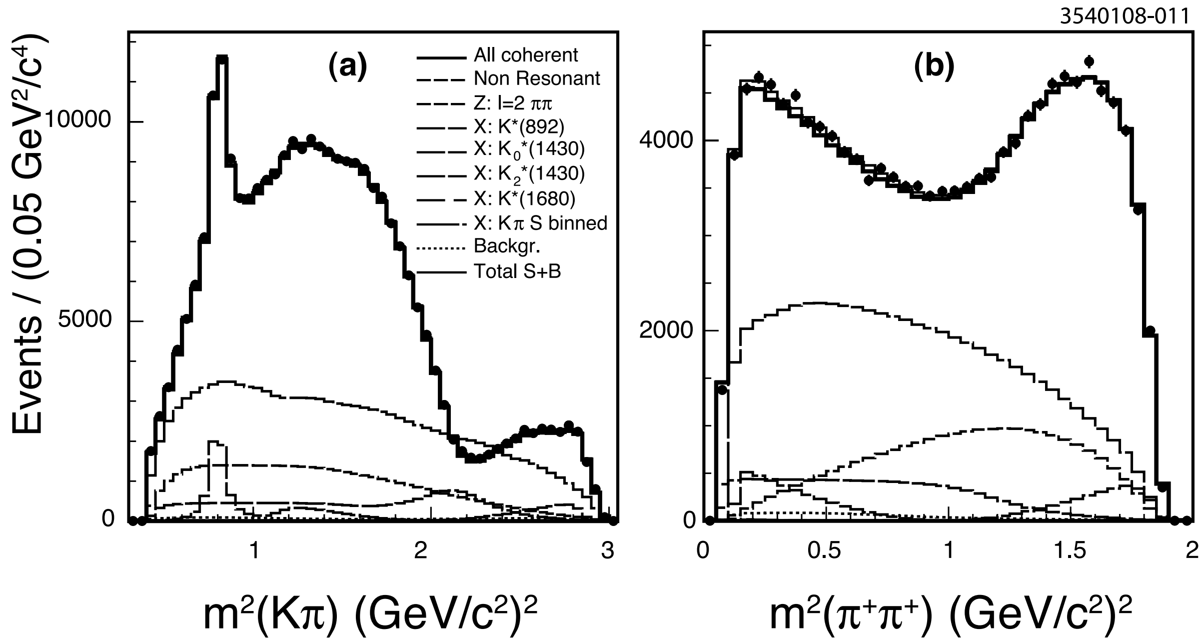

FIG. 11: Projections of the Dalitz plot on (a) $m^2(K\pi)$ (two entries per event), and (b) $m^2(\pi\pi)$ variables for QMIPWA.

VII. DISCUSSION

The $K_0^*(1430)$ parameters which we find in the fit are significantly different from the PDG [8] values which are dominated by the LASS measurement. Our data prefers the

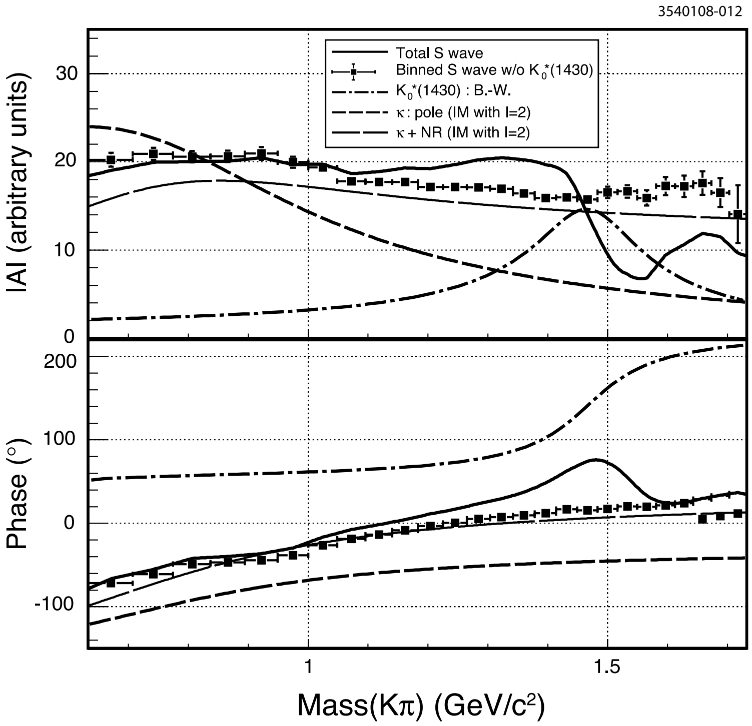

FIG. 12: The magnitude and phase of the $K\pi$ S wave in Model I2 and QMIPWA.

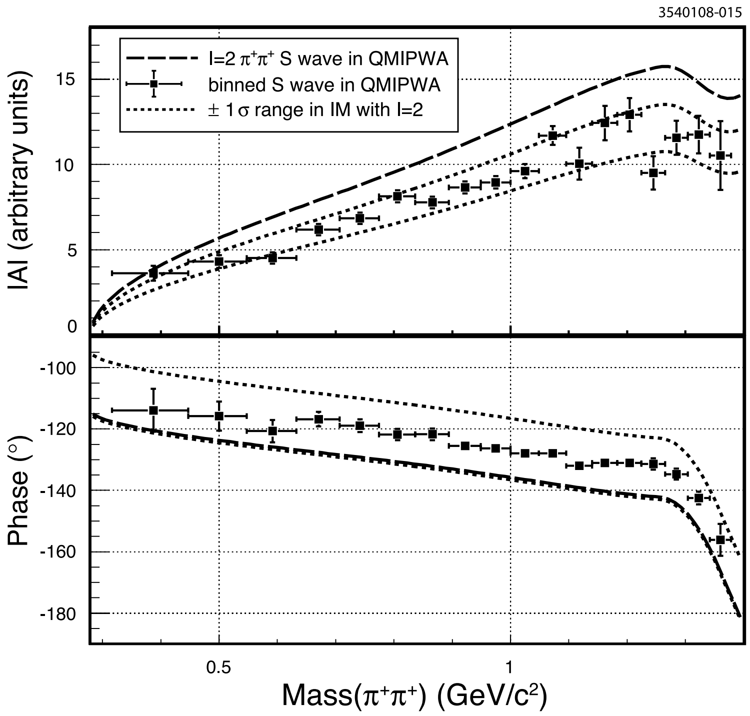

FIG. 13: The magnitude and phase of the $I = 2$ $\pi^+\pi^+$ S wave in Model I2 and QMIPWA.

$K_0^*(1430)$ resonance, that is ~50 MeV/c^2 heavier and about two times narrower. Our result is consistent with E791 [5], and preliminary FOCUS [21] measurements. Possible explana-

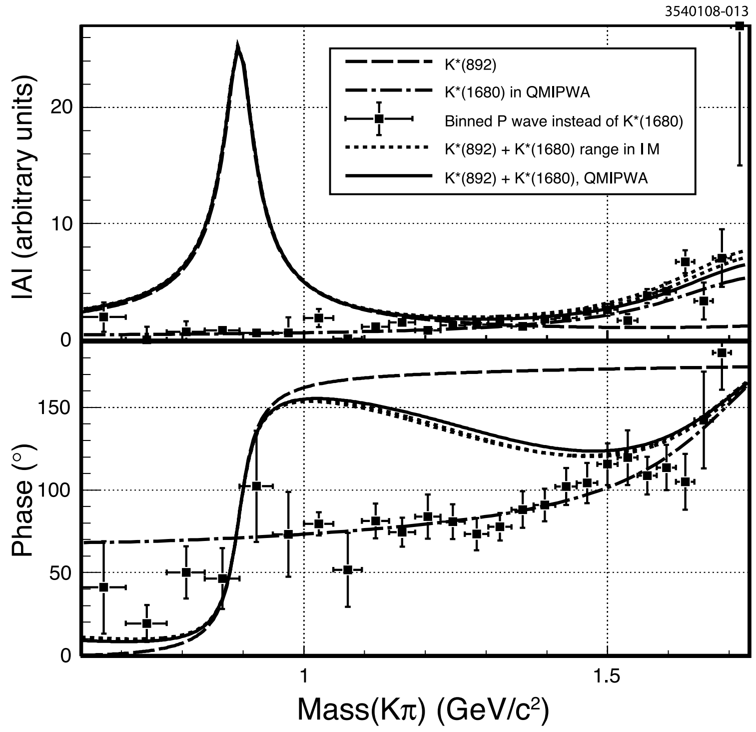

FIG. 14: The magnitude and phase of the $K\pi$ P wave in Model I2 and QMIPWA.

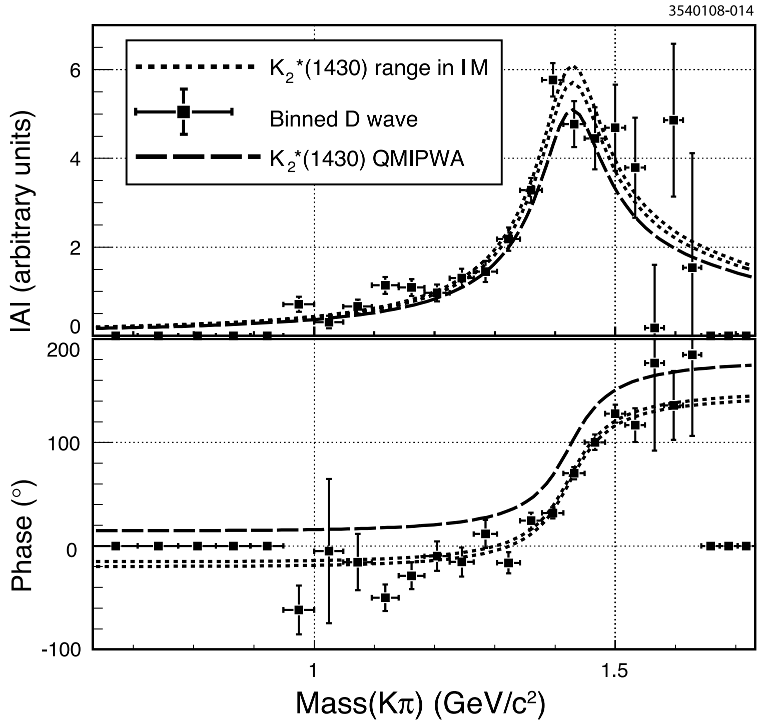

FIG. 15: The magnitude and phase of the $K\pi$ D wave in Model I2 and QMIPWA.

tions include that the $K_0^*(1430)$ resonance parameters depends on its production mechanism which are different in $K\pi$ scattering and D-meson decays, or the $K_0^*(1430)$ parameters are strongly model-dependent. In particular they may depend on interference with other S-wave contributions.

In all of our fits the $K^*(892)$ mass is consistent, but the width is 5 MeV/c^2 smaller than the PDG [8] value. The $K^*(892)$ width in the PDG is an average value over about 20 experimental measurements. Our measurement does not contradict any single result included in PDG. The largest difference is about three standard deviation from the LASS value. We also tested the $K^*(892)$ width model dependence. The largest variation is expected from applying Blatt-Weisskopf form factors. A variation of the radial parameters from zero to four times their nominal values causes a variation in the width of 0.7 MeV/c^2, which cannot explain the large difference with the PDG average. Recent results from FOCUS [22] and Belle [23] also indicate a $K^*(892)$ width smaller than the PDG value.

The S wave and κ pole Gaussian form factors used in E791 [5, 6] may cause an enhancement of the magnitude at low $K\pi$ mass. However, the form factor is a real function and does not change the phase of the complex amplitude. In our measurement we do not use a form factor for S waves, and present results on the total observed amplitude. The measured S-wave magnitude is essentially constant up to 1.4 GeV/c^2. The phase of the complex S-wave amplitude shows smooth variation from –80° at $K\pi$ threshold to 40° at 1.4 GeV/c^2. At higher mass the ampliude is distorted by a contribution from the $K_0^*(1430)$ resonance. Our data require a dominant contribution from the $K\pi$ S wave, which low mass behavior does not support a description as a regular resonance structure.

The S wave is measured in a model independent way, while the P, D waves are parametrized by the Breit-Wigners. In systematic cross checks we add more freedom to the P and D waves but did not find improvement in the fit quality or any significant deviation of the binned wave from the analytic function of the isobar model. These variations of the P and D waves are used in order to estimate model dependence of the S wave. Our systematic uncertainties accounts for possible model dependence of the P and D waves.

We find that the $I = 2$ $\pi^+\pi^+$ S wave is not consistent with a constant term. Its behavior is well modeled by the analytic function, Eq. 31, and is well described by the binned wave.

VIII. SUMMARY

We describe a partial wave analysis of the $D^+ \to K^-\pi^+\pi^+$ events on the Dalitz plot. We use the CLEO-c data set of 572 pb^{-1} of e^+e^- collisions accumulated at the $\psi(3770)$, which corresponds to a sample of 1.6 million D^+D^- pairs produced in the process $e^+e^- \to \psi(3770) \to D^+D^-$. We select 140793 candidate events for the Dalitz plot with a small background of ∼1.1%. We compare our results with the best previous measurements from E791 [5] using the isobar model. Our results agree with the E791 measurement, as shown in Table V for their best model. The fit quality can be improved if we add the $I = 2$ $\pi^+\pi^+$ S-wave contribution, as presented in Table VIII.

We apply a model-independent approach, developed in Ref. [6], to measure the magnitude and phase of the $K\pi$ S wave in the invariant mass range from threshold to the maximum value in this decay. In contrast to E791, we have measured the $K\pi$ S wave without factorization of the form factor for scalar resonances. Our results on the $K\pi$ S-wave phase and magnitude measurement are presented in Table IX and in Fig. 12. The accuracy of the $K\pi$ S-wave measurement is improved, compared to the only previous measurement. We find that the total observed S-wave magnitude in the $D^+ \to K^-\pi^+\pi^+$ decay is essentially constant from $K\pi$ production threshold to ∼1.4 GeV/c^2. The phase shows smooth variation from –80° to

40° in the same range. At higher invariant mass, $m_{K\pi} > 1.4$ GeV/c^2, the S-wave behavior is dominated by the $K_0^*(1430)$ resonance with the possible addition of a nearby higher mass resonances. We find that the P-wave contribution is dominated by $K^*(892)$ and $K^*(1680)$ Breit-Wigner resonances, and the D wave has only a contribution from $K_2^*(1430)$. Using binning techniques, we find no significant deviation of the P and D waves from the isobar model.

In the model-independent approach for the $I = 2$ $\pi^+\pi^+$ S wave we obtain the binned amplitude parameters, listed in Table X, which are consistent with the analytic form of this wave. We find that our data prefers a non-uniform $\pi^+\pi^+$ S wave with a fit fraction of ∼10%. As expected, the $K\pi$ S wave changes slightly with the addition of the $\pi^+\pi^+$ S wave, but the variation is well within our total uncertainties. The addition of the $I = 2$ $\pi^+\pi^+$ S wave to either the isobar model or the model independent partial wave approach is the key piece that gives good agreement with the data in both cases.

Acknowledgments

We gratefully acknowledge the effort of the CESR staff in providing us with excellent luminosity and running conditions. D. Cronin-Hennessy and A. Ryd thank the A.P. Sloan Foundation. This work was supported by the National Science Foundation, the U.S. Department of Energy, the Natural Sciences and Engineering Research Council of Canada, and the U.K. Science and Technology Facilities Council.

---

[1] J. Adler *et al.* (MARK III Collaboration), Phys. Lett. B **196**, 107 (1987).
[2] M.P. Alvarez *et al.* (NA14/2 Collaboration), Z. Phys. C **50**, 11 (1991).
[3] J.C. Anjos *et al.* (E691 Collaboration), Phys. Rev. D **48**, 56 (1993).
[4] P.L. Frabetti *et al.* (E687 Collaboration), Phys. Lett. B **331**, 217 (1994).
[5] E.M. Aitala *et al.* (E791 Collaboration), Phys. Rev. Lett. **89**, 121801 (2002).
[6] E.M. Aitala *et al.* (E791 Collaboration), Phys. Rev. D **73**, 32004 (2006).
[7] R.H. Dalitz, Philos. Mag. **44**, 1068 (1953).
[8] W.-M. Yao *et al.*, Journal of Physics G **33**, 1 (2006).
[9] W. Hoogland *et al.*, Nucl. Phys. B **126**, 109 (1977); N.B. Durusoy *et al.*, Phys. Lett. **45B**, 517 (1973); B.S. Zou *et al.*, published in Hadron 2003 Proceedings, AIP Conf. Proc. 717:347 (2004) [hep-ph/0405118].
[10] G. Viehhauser, Nucl. Instrum. Methods A **462**, 146 (2001); D. Peterson *et al.*, Nucl. Instrum. Methods Phys. Res., Sect. A **478**, 142 (2002); Y. Kubota *et al.*, Nucl. Instrum. Methods Phys. Res., Sect. A **320**, 66 (1992); R.A. Briere *et al.* (CESR-c and CLEO-c Taskforces, CLEO-c Collaboration), Cornell University, LEPP Report No. CLNS 01/1742 (2001) (unpublished).
[11] D. Bugg, hep-ex/0510014.
[12] D. Bugg, Phys. Lett. B **632**, 471 (2006).
[13] J.A. Oller, Phys. Rev. D **71**, 054030 (2005).
[14] S. Dobbs *et al.* (CLEO Collaboration), Phys. Rev. D **76**, 112001 (2007).
[15] D.J. Lange, Nucl. Instrum. Methods Phys. Res., Sect. A **462**, 152 (2001).
[16] S. Kopp *et al.* (CLEO Collaboration), Phys. Rev. D **63**, 092001 (2001).
[17] J.M. Blatt and V.F. Weisskopf, *Theoretical Nuclear Physics*, Wiley, New York, 1951, p.361.

[18] N.A. Tornquist, Z. Phys. C **68**, 674 (1995).
[19] N.N. Achasov and G.N. Shestakov, Phys. Rev. D **67**, 114018 (2003).
[20] B.S. Zou *et al.*, published in Hadron 2003 Proceedings, AIP Conf. Proc. 717:347 (2004).
[21] J.M. Link *et al.* (FOCUS Collaboration), M.R. Pennington, arXiv:0705.2248 (to be submitted to Phys. Lett. B).
[22] J.M. Link *et al.* (FOCUS Collaboration), Phys. Lett. B **621**, 72 (2005).
[23] D. Epifanov *et al.* (Belle Collaboration), arXiv:0706.2231.